


Higher order Cauchy–Born rule based multiscale cohesive zone model and prediction of fracture toughness of silicon thin films

Shingo Urata · Shaofan Li 

Received: 23 March 2016 / Accepted: 16 August 2016 / Published online: 31 August 2016
© Springer Science+Business Media Dordrecht 2016

Abstract In this work, we extend the multiscale cohesive zone model (MCZM) (Zeng and Li in *Comput Methods Appl Mech Eng* 199:547–556, 2010), in which interatomic potential is embedded into constitutive relation to express cohesive law in fracture process zone, to include the hierarchical Cauchy–Born rule in the process zone and to simulate three dimensional fracture in silicon thin films. The model has been applied to simulate fracture stress and fracture toughness of single-crystal silicon thin film by using the Tersoff potential. In this study, a new approach has been developed to capture inhomogeneous deformation inside the cohesive zone. For this purpose, we introduce higher order Cauchy–Born rules to construct constitutive relations for corresponding higher order process zone elements, and we introduce a sigmoidal function supported bubble mode in finite element shape function of those higher order cohesive zone elements to capture the nonlinear inhomogeneous deformation inside the cohesive zone elements. Benchmark tests with simple 3D models have confirmed that the present

method can predict the fracture toughness of silicon thin films. Interestingly, this is accomplished without increasing of computational cost, because the present model does not require quadratic elements to represent heterogeneous deformation, which is the inherent weakness of the previous MCZM model. Quantitative comparisons with experimental results are performed by computing crack propagation in non-notched and initially notched silicon thin films, and it is found that our model can reproduce essential material properties, such as Young’s modulus, fracture stress, and fracture toughness of single-crystal silicon thin films.

Keywords Cohesive zone model · Crack · Fracture toughness · Multiscale simulation · Silicon thin film

1 Introduction

For brittle materials, such as glasses, ceramics and semiconductor materials, crack initiation and propagation are critical problems for their practical applications. To avoid such crucial issue, material compositions are often modified in both atomistic and mesoscopic levels to improve their fracture toughness. For instance, higher strength glass can be attained by adding small amount of raw materials such as sodium carbonate (soda), lime, dolomite, silicon dioxide (silica), aluminium oxide (alumina), etc., to make the commonly-used soda-lime silicate glass (Shegal and Ito 1998), which will have far more improved frac-

S. Urata
Innovative Technology Research Center, Asahi Glass Co.,
Ltd, 1-1 Suehiro-cho, Tsurumi-ku, Yokohama, Kanagawa
230-0045, Japan
e-mail: shingo-urata@agc.com

S. Li (✉) · S. Urata
Department of Civil and Environmental Engineering,
University of California, Berkeley, CA 94720, USA
e-mail: shaofan@berkeley.edu

ture toughness. Fracture resistance of ceramics can be controlled by adding small amount quantities of other components (Terao et al. 2002) or particles (Tamai et al. 2006). Recently, Demetriou et al. (2010) demonstrated that metallic glass of palladium alloy can attain comparable fracture toughness to the toughest materials that have known owing to its enhanced resistance to the shear-band sliding process by adding a specific composition. In addition, it is well known that controlled stress distribution in depth direction, namely tensile and compressive stress layers, makes materials possessing higher resistance to impacts and collisions. In glass industry, these manufacture techniques have been applied to physically and chemically tempered glasses, and it makes glasses more versatile materials in a wide range of applications (McMeeking and Evans 1982; Varshneya 2010; Karlsson et al. 2010; Koike et al. 2012).

Computational simulations can be both helpful and insightful to understand the physical process of fracture and damage, which can help us find the optimal and ultimate modification to the brittle materials and thus accelerate the design and manufacture process. Ab initio and classical molecular dynamics methods provide powerful methods to study fracture by capturing the atomistic bond breakage process in crack tip from atomistic viewpoint (Swiler et al. 1995; Li et al. 2014; Sunyk and Steinmann 2003; Buehler et al. 2006), therefore these methods are the most appropriate, when one needs to optimize atomistic microstructure and composition of materials. However, the present computer and computation technology do not have the resource to attempt such calculations at macroscale. For this reason, multiscale methods, which are abound in ingenuity, have been extensively studied to overcome the large scale gaps in both space and time (Abraham et al. 2000; Tadmor and Miller 2011).

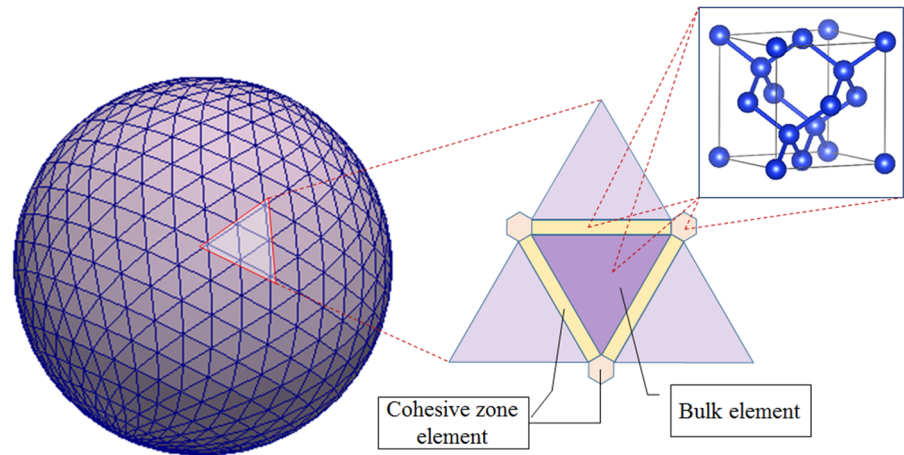
Contrarily, although conventional finite element methods (FEM) are not capable of simulating discontinuity of crack propagation, several innovative technologies based on continuum models have been developed to simulate fracture in recent decades. The eXtended FEM (XFEM) allows us to apply FEM to simulate crack propagation owing to its local enrichment functions, which does not require remeshing during the simulation (Belytschko and Black 1999; Belytschko et al. 2001). Peridynamics is another emerging method, which employs a nonlocal spatial integral equations to model the discontinuous phenom-

ena in non-local media (Siling 2000; Siling et al. 2007; Madenci and Oterkus 2014).

A relatively more established approach to model fracture is the so-called Cohesive Zone Model (CZM) (Shet and Chandra 2002; Volokh 2004) that assumes the presence of a zero-thickness fracture process zone between elements. It enables us to simulate fragmentation of materials and delamination of adhesions by using the empirical traction-separation relations for the process zone. Besides of its empirical cohesive law, the conventional CZM process zone has zero thickness, which limits its ability to simulate mixed mode fracture, and its empirical cohesive law is always inconsistent with the bulk material mechanical responses. To fundamentally resolve these issues, we have developed the Multiscale Cohesive Zone Model (MCZM), which employs atomistic based information to derive the cohesive law, in order to simulate crack propagation with atomistic resolution without any ad-hoc assumptions (Liu et al. 2008; Zeng and Li 2010; He and Li 2012; Qian and Li 2010; Liu and Li 2012; Li et al. 2012; Zeng and Li 2012; Fan et al. 2013; Fan and Li 2015). In this method, the cohesive zone between two bulk elements is modeled as a significantly thin element, and the relation between stress and strain is evaluated by using interatomic potential functions with an unit cell composed of multiple atoms for both cohesive zone (CZ) and bulk elements. Thereby, it is possible to model intrinsic weakness of CZ due to existences of, for instance, defects or mismatch of crystal structure at grain boundary by assuming an interface depletion potential (Zeng and Li 2010; Qian and Li 2010) or higher order deformation in CZ (Fan et al. 2013; Fan and Li 2015).

In this study, we will discuss how to extend the MCZM to three-dimensional calculations for practical applications of the real materials, because previous works have mainly focused on theoretical construction of the MCZM and 2D simulations with relatively simple potential functions. In this work, we select crystal silicon as a model material, because it is the basic functional material for semiconductor devices and extensively used in micro-electromechanical system (MEMS), such as various integrated circuits, microscale sensors, actuators, reactors and so on (Bogue 2007; Jensen 1999). In recent years, we have seen further developments in various sophisticated MEMS structure in order to continuously extending its application range, increasing its efficiency, and con-

Fig. 1 Concepts of hierarchical multiscale cohesive zone model



suming less power and materials, which put further requirements and demands on materials strength and fracture toughness. Since the small material toughness of silicon is crucial for MEMS design, vigorous efforts have been made to measure silicon’s mechanical properties, such as Young’s modulus and fracture toughness, corresponding to specific microscale structures experimentally e.g. [Boyd et al. \(2013\)](#), [Li et al. \(2005\)](#), [Fitzgerald et al. \(2000\)](#), [Nakao et al. \(2008\)](#), [Sundararajan and Bhushan \(2002\)](#), [Chasiotis et al. \(2006\)](#), [Ando et al. \(2005\)](#). In the present study, we would like to take a multiscale computational approach to exam the small scale silicon fracture toughness by considering the interatomic interaction. To do so, we employ Tersoff potential that considers bond order to represent three-body interaction ([Tersoff 1988a, b](#)). Because the Tersoff potential has been widely used in modeling of various important brittle materials in MEMS, such as silicon ([Tersoff 1988b](#)), silicon carbide ([Tersoff 1989](#)), silicon nitride ([de Brito Mota et al. 1998](#)) and silica ([Munetoh et al. 2007](#)), the implementation of the Tersoff potential in MCZM analysis will enhance applicability of the method.

The outline of the paper is as follows: Sect. 2 describes the finite element framework of the MCZM, and proposes definition of CZ element with bubble mode for 3D model. Then, we shall derive equations including the second order stress tensor to implement the Tersoff three-body potential to the MCZM for single-crystal silicon. Sect. 3 demonstrates usefulness of the bubble mode by using relatively simple 3D models, and shows numerical results for Young’s modu-

lus and the fracture stress by using the Tersoff potential. After illustrating the main concepts, detailed simulation and quantitative comparison with experiments of fracture toughness measurements for thin single-crystal silicon film is performed in Sect. 4. Finally, some concluding remarks are given in Sect. 5. Some detailed derivatives and formulations are provided in “Appendix”.

2 Multiscale cohesive zone model (MCZM) and its FEM formulation

We start by reviewing the multiscale cohesive zone model and formulating the finite element formulation of the multiscale cohesive zone model (MCZM).

2.1 Hierarchical Cauchy–Born rule based MCZM

In the MCZM, the entire domain of the specimen is discretized by a number of bulk elements as the usual finite element (FEM) discretization, and the cohesion zone is represented by a network of cohesive zone elements among bulk elements, see Fig. 1. However, unlike conventional cohesive zone model, the cohesive zone (CZ) or the process zone in MCZM is represented by an element with extremely thin but finite thickness. In this work, since the tetrahedral element is utilized for the bulk element, the cohesive zone element is represented by a triangular-shaped prism element which shares two triangular facets of the two adjacent tetrahedral (bulk) elements as shown in Fig. 2.

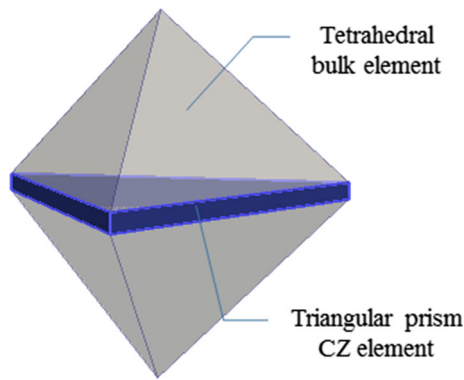


Fig. 2 Wedge shape cohesive zone element with two tetrahedral bulk elements

Another important characteristic of MCZM is that the strain-stress relation is derived based on the Cauchy–Born (CB) rule that is evaluated by deformation of a unit cell, which is embedded in each quadrature point in both bulk and CZ elements.

The key feature of the so-called hierarchical MCZM is that the different order of the Cauchy–Born rule is applied to different order of the cohesive zones. We denote the bulk element as the zero-th order cohesive zone, the interphase element between two bulk elements as the first order cohesive zone, and void among the multiple bulk elements and interphase elements as the third order or even fourth order cohesive zone elements [see Li et al. (2014) for details].

Consider the finite deformation of a crystalline lattice. We may be able to express any deformed position vector in the current configuration by its undeformed image in the referential configuration through Taylor expansion,

$$\begin{aligned} \Delta \mathbf{x} = & \frac{\partial \mathbf{x}}{\partial \mathbf{X}} \Big|_{\mathbf{x}=\mathbf{x}_A} \cdot \Delta \mathbf{X} + \frac{1}{2!} \frac{\partial^2 \mathbf{x}}{\partial \mathbf{X}^2} \Big|_{\mathbf{x}=\mathbf{x}_A} : \Delta \mathbf{X} \otimes \Delta \mathbf{X} \\ & + \frac{1}{3!} \frac{\partial^3 \mathbf{x}}{\partial \mathbf{X}^3} \Big|_{\mathbf{x}=\mathbf{x}_A} : \Delta \mathbf{X} \otimes \Delta \mathbf{X} \otimes \Delta \mathbf{X} + \dots \end{aligned} \quad (1)$$

or in a more common notation,

$$\begin{aligned} \Delta \mathbf{x} = & \mathbf{F}_A \cdot \Delta \mathbf{X} + \frac{1}{2!} \mathbf{G}_A : \Delta \mathbf{X} \otimes \Delta \mathbf{X} \\ & + \frac{1}{3!} \mathbf{H}_A : \Delta \mathbf{X} \otimes \Delta \mathbf{X} \otimes \Delta \mathbf{X} + \dots \end{aligned} \quad (2)$$

where

$$\mathbf{F}_A := \frac{\partial \mathbf{x}}{\partial \mathbf{X}} \Big|_{\mathbf{x}=\mathbf{x}_A}$$

is the deformation gradient, and

$$\mathbf{G}_A := \frac{\partial^2 \mathbf{x}}{\partial \mathbf{X}^2} \Big|_{\mathbf{x}=\mathbf{x}_A} \quad \text{and} \quad \mathbf{H}_A := \frac{\partial^3 \mathbf{x}}{\partial \mathbf{X}^3} \Big|_{\mathbf{x}=\mathbf{x}_A}$$

are the second and the third gradient of \mathbf{F} .

The above expression is often referred to as the higher order Cauchy–Born rule e.g. Sunyk and Steinmann (2003). The so-called hierarchical MCZM is that it uses the first order Cauchy–Born rule,

$$\Delta \mathbf{x} \approx \mathbf{F}_A \cdot \Delta \mathbf{X},$$

to derive the stress-strain relation in the bulk crystal element, i.e. the zero-th order cohesive zone; and it uses the second order Cauchy–Born rule,

$$\Delta \mathbf{x} \approx \mathbf{F}_A \cdot \Delta \mathbf{X} + \mathbf{G}_A : \Delta \mathbf{X} \otimes \Delta \mathbf{X},$$

to derive the stress-strain relation in the first cohesive zone element, and it uses the third order Cauchy–Born rule,

$$\Delta \mathbf{x} \approx \mathbf{F}_A \cdot \Delta \mathbf{X} + \mathbf{G}_A : \Delta \mathbf{X} \otimes \Delta \mathbf{X} + \mathbf{H}_A : \Delta \mathbf{X} \otimes \Delta \mathbf{X} \otimes \Delta \mathbf{X}$$

to derive the constitutive relation in the second order cohesive zone element; and so on and so forth. In this work, we restrict our attention to only the bulk element and the interphase element, i.e. the first order cohesive zone element.

For single-crystal silicon, it is not a Bravais lattice, and the unit cell of silicon is composed of a multiple atoms. The silicon lattice structure is that diamond cubic structure. With considering shape change of the unit cell associated with each element deformation, we can evaluate the first Piola–Kirchhoff stress tensor \mathbf{P} and the second order stress tensor \mathbf{Q} as derivatives of strain energy density W computed with Tersoff potential as shown in 2.4.

2.2 Multiscale finite element formulation of MCZM

Here we briefly derive the Galerkin weak formulation based on virtual work principle for FEM implementation. The details can be found in our previous works (Zeng and Li 2010; He and Li 2012; Qian and Li 2010; Liu and Li 2012; Li et al. 2012; Zeng and Li 2012; Fan et al. 2013; Fan and Li 2015). At first, the Lagrangian of the continuum system is defined as,

$$\mathcal{L} = \mathcal{K} - (\mathcal{W}_{int} + \mathcal{W}_{ext}) \quad (3)$$

where \mathcal{W}_{ext} is the external potential energy. \mathcal{W}_{int} and \mathcal{K} are the strain energy of the continuum and total kinetic energy, respectively, and defined as,

$$\mathcal{K} = \int_{\Omega} \frac{1}{2} \rho \dot{\mathbf{u}} \cdot \dot{\mathbf{u}} dV \tag{4}$$

$$\mathcal{W}_{int} = \int_{\Omega} W(\mathbf{F}, \mathbf{G}) dV \tag{5}$$

ρ and $\dot{\mathbf{u}}$ are the mass density and velocity field of the continuum, respectively. W is the strain energy density function as functions of strain and strain gradient.

Then, the Hamiltonian principle can be applied to derive the variational weak formulation,

$$\int_{t_0}^{t_1} \left(\delta \mathcal{K} - (\delta \mathcal{W}_{int} + \delta \mathcal{W}_{ext}) \right) dt = 0, \tag{6}$$

where

$$\begin{aligned} \int_{t_1}^{t_2} \delta \mathcal{K} dt &= \int_{t_1}^{t_2} \int_{\Omega} \rho \dot{\mathbf{u}} \cdot \delta \dot{\mathbf{u}} dV dt \\ &= - \int_{t_1}^{t_2} \int_{\Omega} \rho \ddot{\mathbf{u}} \cdot \delta \mathbf{u} dV dt \end{aligned} \tag{7}$$

$$\begin{aligned} \delta \mathcal{W}_{int} &= \int_{\Omega} \left[\frac{\partial W}{\partial \mathbf{F}} : \delta \mathbf{F} + \frac{\partial W}{\partial \mathbf{G}} : \delta \mathbf{G} \right] dV \\ &= \int_{\Omega} \left[\mathbf{P} : \delta \mathbf{F} + \mathbf{Q} : \delta \mathbf{G} \right] dV \end{aligned} \tag{8}$$

$$\delta \mathcal{W}_{ext} = - \int_{\Omega} \mathbf{b} \cdot \delta \mathbf{u} dV - \int_{\delta \Omega_t} \bar{\mathbf{T}} \cdot \delta \mathbf{u} dS \tag{9}$$

In Eq. (9), \mathbf{b} and $\bar{\mathbf{T}}$ are the body force inside the bulk media and the traction vector on the surface $\delta \Omega_t$, respectively. Consequently, the Galerkin weak formulation can be reformulated in terms of element summation as follows.

$$\begin{aligned} &\mathbf{A} \left\{ \int_{\Omega_B^e} \left(\rho_0 \ddot{\mathbf{u}}^h \cdot \delta \mathbf{u} + \mathbf{P} : \delta \mathbf{F}^h \right) dV \right\} \\ &+ \mathbf{A} \left\{ \int_{\Omega_C^e} \left(\mathbf{P} : \delta \mathbf{F}^h + \mathbf{Q} : \delta \mathbf{G}^h \right) dV \right\} \\ &= \frac{n_B^e}{\mathbf{A}} \left\{ \int_{\Omega_B^e} \mathbf{b} \cdot \delta \mathbf{u}^h dV \right\} + \frac{n_C^e}{\mathbf{A}} \left\{ \int_{\Omega_C^e} \mathbf{b} \cdot \delta \mathbf{u}^h dV \right\} \\ &+ \mathbf{A} \left\{ \int_{\Gamma_t} \bar{\mathbf{T}} \cdot \delta \mathbf{u}^h dS \right\} \end{aligned} \tag{10}$$

where, Ω_B^e and Ω_C^e are the domains of bulk and CZ elements; Γ_t is the traction boundary of the system; n_B^e and n_C^e are number of bulk and CZ elements, respectively, and superscript h represents kinetic field corresponding to FEM interpolation field. Note that only the bulk element is assumed to have constant deformation gradient, while all cohesive elements are assumed to have up to the second order deformation gradient, i.e. the

first gradient of the deformation gradient, which will be discussed in details in later sections.

By considering FEM interpolation approximation, displacement field can be represented by using element shape function matrix \mathbf{N} as follows,

$$\mathbf{u}^h(\mathbf{X}) = \sum_{i=1}^{n_{node}} \mathbf{N}_i(\mathbf{X}) \mathbf{d}_i. \tag{11}$$

where n_{node} is number of node composing an element, and \mathbf{d} is the nodal displacement vector. According to Eqs. (10) and (11), the discrete equation of motion for FEM procedure is expressed as,

$$\mathbf{M} \ddot{\mathbf{d}} + \mathbf{f}^{int}(\mathbf{d}) - \mathbf{f}^{cohe}(\mathbf{d}) = \mathbf{f}^{ext} \tag{12}$$

where, \mathbf{M} is the mass matrix. \mathbf{f}^{int} , \mathbf{f}^{cohe} and \mathbf{f}^{ext} are force vectors from bulk elements, CZ elements and external force, respectively. They are defined as follows:

$$\mathbf{M} = \mathbf{A} \sum_{e=1}^{n_B^e} \int_{\Omega_B^e} \rho_0 \mathbf{N}^e T \mathbf{N}^e dV \tag{13}$$

$$\mathbf{f}^{int} = \mathbf{A} \sum_{e=1}^{n_B^e} \int_{\Omega_B^e} \mathbf{B}^e T \mathbf{P}^e(\mathbf{d}) dV \tag{14}$$

$$\mathbf{f}^{ext} = \mathbf{A} \left\{ \int_{\Omega_B^e} \mathbf{N}^e T \mathbf{B}^e dV + \int_{\delta \Gamma_t} \mathbf{N}^e T \bar{\mathbf{T}}^e dS \right\} \tag{15}$$

$$\mathbf{f}^{cohe} = \mathbf{A}^{CZ} \sum_{e=1}^{n_{elem}} \int \left\{ \mathbf{B}^e T \mathbf{P}^e(\mathbf{d}) + \mathbf{C}^e T \mathbf{Q}^e(\mathbf{d}) \right\} dV \tag{16}$$

where, \mathbf{B}^e and \mathbf{C}^e are the element strain-displacement matrix and the gradient of the strain-displacement matrix, respectively. The explicit time integration based Newmark- β method with $\beta = 0$ (Belytschko 1983) is used in nodal velocity and displacement updates.

Figure 3 shows nodes of the triangular prism elements and the Gauss integration points in the elements. For the wedge element, we apply the following isoparametric shape function with bubble mode, in order to describe second order deformation adequately. It is of course possible to employ quadratic elements for both bulk and CZ elements, however it requires more expensive computation. Instead of doing that, we nevertheless add only one bubble mode in the center of CZ element to minimize increasing computational cost for the occasion to apply MCZM to more complex or amorphous materials. The complete set of shape functions are,

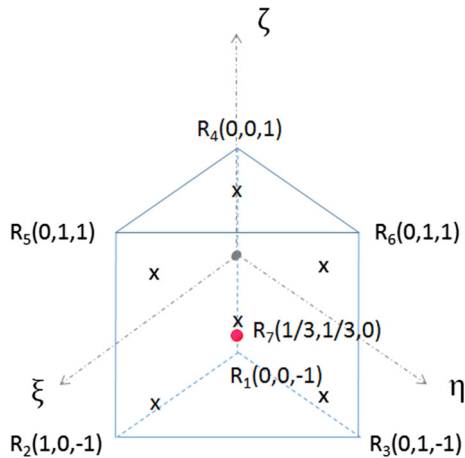


Fig. 3 Six nodes of isoparametric triangular prism element and a bubble node. Red circle is the point of a bubble node, and the cross indicates six Gauss integration points; $(1/6, 1/6, \pm 1/\sqrt{3})$, $(1/6, 2/3, \pm 1/\sqrt{3})$, $(2/3, 1/6, \pm 1/\sqrt{3})$

$$\left. \begin{aligned}
 N_1 &= \frac{1}{2}(1 - \xi - \eta)(1 - \zeta) - \frac{1}{6}N_7 \\
 N_2 &= \frac{1}{2}\xi(1 - \zeta) - \frac{1}{6}N_7 \\
 N_3 &= \frac{1}{2}\eta(1 - \zeta) - \frac{1}{6}N_7 \\
 N_4 &= \frac{1}{2}(1 - \xi - \eta)(1 + \zeta) - \frac{1}{6}N_7 \\
 N_5 &= \frac{1}{2}\xi(1 + \zeta) - \frac{1}{6}N_7 \\
 N_6 &= \frac{1}{2}\eta(1 + \zeta) - \frac{1}{6}N_7 \\
 N_7 &= 27(1 - \xi - \eta)\xi\eta(1 - \zeta)(1 + \zeta)
 \end{aligned} \right\} \text{Shape functions} \tag{17}$$

Then, according to the shape functions, the first and second order deformation gradients are expressed as,

$$\mathbf{F} = \mathbf{I} + \frac{\partial \mathbf{N}}{\partial \mathbf{X}} \cdot \mathbf{d} = \mathbf{I} + \mathbf{B} \cdot \mathbf{d} \tag{18}$$

$$\mathbf{G} = \frac{\partial^2 \mathbf{N}}{\partial \mathbf{X} \otimes \partial \mathbf{X}} \cdot \mathbf{d} = \mathbf{C} \cdot \mathbf{d} \tag{19}$$

where

$$\mathbf{B} := \left[\frac{\partial \mathbf{N}}{\partial \mathbf{X}} \right], \text{ and } \mathbf{C} := \left[\frac{\partial^2 \mathbf{N}}{\partial \mathbf{X} \otimes \partial \mathbf{X}} \right].$$

We note in passing that the bubble mode approach can be also used for the second order cohesive element, which is involved with the third order Cauchy–Born rule; and it needs some cubic order polynomials to support the second order gradient of the deformation gradient \mathbf{F} . In the Appendix, we listed the bubble function for a complete isoparametric quadratic interpolation functions for a prism element.

The thickness of CZ elements (t_{CZ}) is defined by using a representative length (L) associated with area of the triangular facet (A_{Tri}),

$$t_{CZ} = p_{th} \times L = p_{th} \times 2 \left(\frac{A_{Tri}}{\sqrt{3}} \right)^{1/2} \tag{20}$$

where the parameter L is length of a side if the triangular facet is assumed as an equilateral triangle. Here, a scale parameter p_{th} is introduced, which is in a range from 0.001 to 0.1. The reason why the CZ thickness depends on the area of facet of the tetrahedron bulk element is because the thickness of the CZ element should be small enough compared with the characteristic length of the bulk element that it is associated to. Usually, we assume that the thickness of CZ element is a scale factor multiplying the characteristic length of the bulk element. On the other hand, if the bulk element is a regular tetrahedron, meaning that its all four facets are equilateral triangles, then the characteristic length of tetrahedron can be associated the area of the equilateral triangle. At the same time, the scale parameter should be small enough such that the discrete medium will not have obvious dispersion, which makes the MCZM mesh close to the physical reality that it tries to approximate.

Alternative to Eq. (16), the internal cohesive force can be also evaluated by using integration of parts as discussed in Fan and Li (2015),

$$\begin{aligned}
 \int_{\Omega} (\mathbf{P}(\phi) : \delta \mathbf{F} + \mathbf{Q}(\phi) : \delta \mathbf{G}) dV &= - \int_{\Omega} (\nabla_x \cdot (\mathbf{P} - \nabla_x \mathbf{Q})) \cdot \delta \mathbf{x} dV \\
 + \int_{\partial \Omega} (\mathbf{P} - \nabla_x \cdot \mathbf{Q}) : (\mathcal{N} \otimes \delta \mathbf{x}) dS &+ \int_{\partial \Omega} \mathbf{Q} : (\mathcal{N} \otimes \delta \mathbf{F}) dS
 \end{aligned} \tag{21}$$

where, Ω is domain of CZ element, and \mathcal{N} is normal vector of the facet of CZ element. Observing Eq. (21), the first term of the right-hand side (RHS) will disappear because it is part of the equation of motion in the cohesive zone. The second and third terms of RHS are boundary conditions, and the third term is the boundary condition for the second order stress tensor, which we often neglect because of its numerical insignificance. Note that these boundary conditions are in fact the interface boundary conditions between the bulk crystal element and the cohesive zone element.

By using divergence theorem, the second term can be converted to a surface integral on the interface between the bulk crystal element and the cohesive zone element, and we can then define a higher order interface traction vector,

$$\mathbf{T} = (\mathbf{P} - \nabla_X \cdot \mathbf{Q}) \cdot \mathcal{N}. \tag{22}$$

Thus, according to Eqs. (14)–(16) and (22), it is possible to express interfacial cohesive relation by using only atomistic potential, instead of using the empirical formulation e.g. Xu and Needleman (1994). By doing so, we can derive the traction-separation based on first-principle while working in the framework of the macroscale continuum modeling. Thus the proposed higher order Cauchy–Born rule based MCZM provides great advantage to examine fracture toughness of materials whose experimental data is not available.

2.3 Higher order Cauchy–Born rule in crystal lattices

We now apply the higher order Cauchy–Born rule discussed in the previous section to crystal lattices in different type of cohesive elements (see Fig. 4).

In this work, we only consider the crystal structure of silicon, which is a type of diamond cubic, i.e. $Fd3m$. It may be viewed as the intrusion of two FCC lattices, α and β (Fig. 5). Hence, the inner displacements between two lattices can be defined as a vector \mathbf{v} from the first lattice α to another β (Tadmor et al. 1999; Khoei et al. 2014; Park and Klein 2008; Khoei and DorMohammadi 2012; Tang et al. 2006).

When evaluating stress based the Tersoff Potential, we only take the nearest four atoms into account to calculate interactions, the strain energy density and its derivative can be calculated by the pseudo unit cell composed of five atoms. The nearest four atoms, which composed of a tetrahedral structure with the central atom, all belong to a different FCC lattice unit cell β from the FCC lattice α to which the center silicon resides (Fig. 5). If we term the central atom as index 1, and others are from 2 to 5, distances of atoms are defined as,

$$r_{1j} = |\mathbf{r}_{1j}| = |\mathbf{r}_1 - \mathbf{r}_j - \mathbf{v}| \quad j = 2, 3, \dots, 5 \tag{23}$$

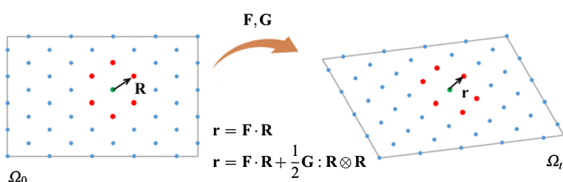


Fig. 4 Illustration of higher order Cauchy–Born rule in crystal lattices

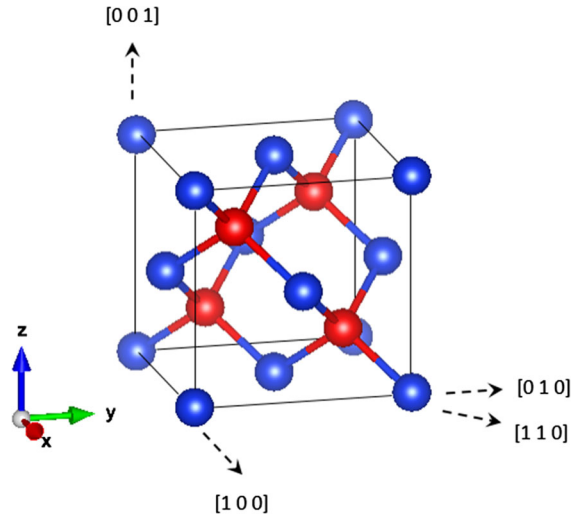


Fig. 5 Unit cell of silicon crystal diamond cubic. Red and blue colors indicate atoms belong to two different FCC lattices

$$r_{jk} = |\mathbf{r}_{jk}| = |\mathbf{r}_j - \mathbf{r}_k| \quad j, k = 2, 3, \dots, 5, \text{ and } j \neq k \tag{24}$$

The vector \mathbf{v} can be evaluated to minimize strain energy density as shown in “Appendix”. It had been found that the optimization of vector \mathbf{v} is crucial to figure out the most stable configuration of atoms at each deformation (Tadmor et al. 1999).

Because overall non-uniform deformation field can be interpreted by a set of bulk elements with piece-wise uniform deformations, we can assume the first order Cauchy–Born rule to represent deformation of the bulk element.

$$\mathbf{r}_i = \mathbf{F} \mathbf{R}_i \tag{25}$$

where, \mathbf{R}_i is original position of atom i in the unit cell, and \mathbf{r}_i is the position after deformation. \mathbf{F} is the first order deformation gradient of each element.

$$\mathbf{F} = \frac{\partial \mathbf{x}}{\partial \mathbf{X}} \tag{26}$$

On the other hand, CZ elements that connect the bulk elements support nonlinear and non-uniform deformation, and thus higher order deformation gradient should be taken into account when calculating stress in the CZ element. Indeed, it has been already confirmed that the effect of second order deformation will weaken CZ element in 2D model (Fan et al. 2013; Fan and Li 2015). In this study, we have applied the same technique to the 3D cohesive zone element by considering the second order deformation gradient, where the presence of

the non-uniform deformation is postulated. Thus, atom position can be expressed by using the second order deformation gradient tensor \mathbf{G} ,

$$\mathbf{r}_i = \mathbf{F}\mathbf{R}_i + \frac{1}{2}\mathbf{G} : (\mathbf{R}_i \otimes \mathbf{R}_i) \tag{27}$$

$$\mathbf{G} = \frac{\partial \mathbf{F}}{\partial \mathbf{X}} = \frac{\partial^2 \mathbf{x}}{\partial \mathbf{X} \otimes \partial \mathbf{X}} \tag{28}$$

2.4 Tersoff potential

The strain energy density W can be written as follows,

$$W = \frac{U_1}{\Omega_0} = \frac{1}{2\Omega_0} \sum_{j=2}^5 V_{1j} \tag{29}$$

where, U_1 is the potential energy for the central atom 1, and Ω_0 is the volume occupied by an atom in the initial configuration. V_{1j} is the Tersoff potential energy between the central atom 1 and a surrounding atom j as

$$V_{1j} = f_C(r_{1j})[f_R(r_{1j}) + b_{1j}f_A(r_{1j})] \tag{30}$$

In the Tersoff potential, the functions f_R, f_A are,

$$f_R(r_{1j}) = A \exp(-\lambda_{1j}r_{1j}) \tag{31}$$

$$f_A(r_{1j}) = -B \exp(-\mu_{1j}r_{1j}) \tag{32}$$

and the cut off function f_C is defined as follows;

$$f_C(r_{1j}) = \begin{cases} 1 & r_{1j} \leq R_{1j} \\ \frac{1}{2} + \frac{1}{2} \cos\left(\frac{\pi(r_{1j}-R_{1j})}{S_{1j}-R_{1j}}\right) & R_{1j} < r_{1j} < S_{1j} \\ 0 & r_{1j} \geq S_{1j} \end{cases} \tag{33}$$

Note here that, second derivative of the original cutoff function (33) is discontinuous, it is thus unfavorable to estimate inner vector \mathbf{v} at the transition points $r = R_{1j}$ and $r = S_{1j}$. To resolve this issue, (Izumi and Sakai 2004) introduced the dumping cutoff function as;

$$f_C(r_{1j}) = \frac{1}{2} - \frac{1}{2} \tanh\left[\frac{\pi}{2}\left(\frac{r_{1j}-R_{1j}}{S_{1j}-R_{1j}}\right)\right] \tag{34}$$

In this study, we employ the modified cutoff function of Eq. (34) instead of Eq. (33) without changing parameters R_{1j} and S_{1j} of the original Tersoff potential.

By taking account three body interaction, the parameter b_{1j} in Eq. (30) will explicitly depend on the location of the third atom k as follows,

$$b_{1j} = \left(1 + \beta^n \zeta_{1j}^n\right)^{\frac{-1}{2n}} \tag{35}$$

$$\zeta_{1j} = \sum_{k \neq i,j}^5 f_c(r_{1k})g(\theta_{1jk}) \tag{36}$$

$$g(\theta_{1jk}) = 1 + \frac{c^2}{d^2} - \frac{c^2}{d^2 + (h - \cos\theta_{1jk})^2} \tag{37}$$

$$\cos\theta_{1jk} = \frac{\mathbf{r}_{1j}\mathbf{r}_{1k}}{r_{1j}r_{1k}} = \frac{(r_{1j}^2 + r_{1k}^2 - r_{jk}^2)}{2r_{1j}r_{1k}} \tag{38}$$

The parameter set of the Tersoff potential used in this study is adopted from Tersoff’s second paper (Tersoff 1988b), which can reproduce elastic properties of silicon more accurately.

According to the expression of the potential energy density, the first Piola-Kirchhoff stress tensor can be derived as,

$$\begin{aligned} \mathbf{P} &= \frac{\partial W}{\partial \mathbf{F}} = \frac{1}{2\Omega_0} \frac{\partial}{\partial \mathbf{F}} \left(\sum_{j=2}^5 V_{1j} \right) \\ &= \frac{1}{2\Omega_0} \sum_{j=2}^5 \left(\frac{\partial V_{1j}}{\partial \mathbf{F}} + \frac{\partial V_{1j}}{\partial \mathbf{v}} \frac{\partial \mathbf{v}}{\partial \mathbf{F}} \right). \end{aligned} \tag{39}$$

The inner displacement \mathbf{v} can be evaluated by minimizing of the strain energy density W , i.e.

$$\left(\frac{\partial V_{1j}}{\partial \mathbf{v}}\right)_{\mathbf{F}} = 0. \tag{40}$$

This condition is achieved by using Newton-Raphson method to find the minimum of the strain energy density, and as a result, the inner displacement vector \mathbf{v} can be obtained. The detailed procedure is presented and documented in ‘‘Appendix’’. Finally, we have

$$\begin{aligned} \mathbf{P} &= \frac{1}{2\Omega_0} \sum_{j=2}^5 \left(\frac{\partial V_{1j}}{\partial \mathbf{F}} \right) \\ &= \frac{1}{2\Omega_0} \sum_{j=2}^5 \left[\frac{\partial V_{1j}}{\partial r_{1j}} \frac{\partial r_{1j}}{\partial \mathbf{F}} \right. \\ &\quad \left. + \sum_{k=2, k \neq j}^5 \left(\frac{\partial V_{1j}}{\partial r_{1k}} \frac{\partial r_{1k}}{\partial \mathbf{F}} + \frac{\partial V_{1j}}{\partial \cos\theta_{1jk}} \frac{\partial \cos\theta_{1jk}}{\partial \mathbf{F}} \right) \right] \end{aligned} \tag{41}$$

where,

$$\begin{aligned} \frac{\partial r_{ij}}{\partial \mathbf{F}} &= \frac{\partial r_{ij}}{\partial \mathbf{r}_{ij}} \frac{\partial \mathbf{r}_{ij}}{\partial \mathbf{F}} = \frac{\mathbf{r}_{ij} \otimes \mathbf{R}_{ij}}{r_{ij}} \tag{42} \\ \frac{\partial \cos\theta_{1jk}}{\partial \mathbf{F}} &= \left(\frac{1}{r_{1k}} - \frac{\cos\theta_{1jk}}{r_{1j}} \right) \frac{\partial r_{1j}}{\partial \mathbf{F}} \end{aligned}$$

$$+ \left(\frac{1}{r_{1j}} - \frac{\cos\theta_{1jk}}{r_{1k}} \right) \frac{\partial r_{1k}}{\partial \mathbf{F}} - \left(\frac{r_{jk}}{r_{1j}r_{1k}} \right) \frac{\partial r_{jk}}{\partial \mathbf{F}} \tag{43}$$

According to Eq. (30), the derivative of V_{1j} with respect to distance r is

$$\begin{aligned} \frac{\partial V_{1j}}{\partial r_{1j}} &= \frac{\partial f_C}{\partial r_{1j}} (f_R(r_{1j}) + b_{1j} f_A(r_{1j})) \\ &+ f_C(r_{1j}) \left(\frac{\partial f_R(r_{1j})}{\partial r_{1j}} + b_{1j} \frac{\partial f_A(r_{1j})}{\partial r_{1j}} \right) \end{aligned} \tag{44}$$

where

$$\frac{\partial f_C(r_{1j})}{\partial r_{1j}} = -\frac{\pi}{4(S_{1j} - R_{1j})} \cosh \left[\frac{\pi(r_{1j} - R_{1j})}{2(S_{1j} - R_{1j})} \right] \tag{45}$$

$$\frac{\partial f_R(r_{1j})}{\partial r_{1j}} = -A\lambda_{1j} \exp(-\lambda_{1j}r_{1j}) \tag{46}$$

$$\frac{\partial f_A(r_{1j})}{\partial r_{1j}} = B\mu_{1j} \exp(-\mu_{1j}r_{1j}). \tag{47}$$

Similarly we can take derivatives of V_{1j} with respect to r_{1k} and θ_{1jk} to estimate Eq. (41), and they are,

$$\begin{aligned} \frac{\partial V_{1j}}{\partial r_{1k}} &= f_C(r_{1j}) f_A(r_{1j}) \left[-\frac{1}{2} (1 + \beta^n \zeta_{1j}^n)^{\frac{1}{2n}-1} \right] \beta^n \zeta_{1j}^{n-1} \\ &\times \frac{\partial f_C(r_{1k})}{\partial r_{1k}} g(\theta_{1jk}) \end{aligned} \tag{48}$$

$$\begin{aligned} \frac{\partial V_{1j}}{\partial \cos\theta_{1jk}} &= f_C(r_{1j}) f_A(r_{1j}) \left[-\frac{1}{2} (1 + \beta^n \zeta_{1j}^n)^{\frac{1}{2n}-1} \right] \beta^n \zeta_{1j}^{n-1} \\ &\times f_C(r_{1k}) \frac{2c^2(\cos\theta_{1jk} - h)}{[d^2 + (h - \cos\theta_{1jk})^2]^2}. \end{aligned} \tag{49}$$

2.5 Second order stress tensor

Next, the second order stress tensor \mathbf{Q} is defined as the derivative of strain energy by the gradient of deformation gradient \mathbf{G} , which is a measure of strain gradient in finite deformation. Analogous to the case of the first Piola–Kirchhoff stress tensor Eq. (41), the second order stress is defined as the conjugate variable of the strain gradient \mathbf{G} ,

$$\begin{aligned} \mathbf{Q} &= \frac{\partial W}{\partial \mathbf{G}} = \frac{1}{2\Omega_0} \frac{d}{d\mathbf{G}} \left(\sum_{j=2}^5 V_{1j} \right) \\ &= \frac{1}{2\Omega_0} \sum_{j=2}^5 \left(\frac{\partial V_{1j}}{\partial \mathbf{G}} + \frac{\partial V_{1j}}{\partial \mathbf{v}} \frac{\partial \mathbf{v}}{\partial \mathbf{G}} \right) \end{aligned}$$

$$\begin{aligned} &= \frac{1}{2\Omega_0} \sum_{j=2}^5 \left[\frac{\partial V_{1j}}{\partial r_{1j}} \frac{\partial r_{1j}}{\partial \mathbf{G}} \right. \\ &\left. + \sum_{k=2, k \neq j}^5 \left(\frac{\partial V_{1j}}{\partial r_{1k}} \frac{\partial r_{1k}}{\partial \mathbf{G}} + \frac{\partial V_{1j}}{\partial \cos\theta_{1jk}} \frac{\partial \cos\theta_{1jk}}{\partial \mathbf{G}} \right) \right] \end{aligned} \tag{50}$$

Here, we again assume that $(\partial V_{1j}/\partial \mathbf{v})_{\mathbf{G}} = 0$ with minimizing the strain energy [see Eq. (40)], and, in this equation, we have

$$\frac{\partial r_{ij}}{\partial \mathbf{G}} = \frac{\partial r_{ij}}{\partial \mathbf{r}_{ij}} \frac{\partial \mathbf{r}_{ij}}{\partial \mathbf{G}} = \frac{\mathbf{r}_{ij} \otimes \mathbf{R}_{ij} \otimes \mathbf{R}_{ij}}{2r_{ij}} \tag{51}$$

and

$$\begin{aligned} \frac{\partial \cos\theta_{1jk}}{\partial \mathbf{G}} &= \frac{\partial \cos\theta_{1jk}}{\partial r_{1j}} \frac{\partial r_{1j}}{\partial \mathbf{G}} + \frac{\partial \cos\theta_{1jk}}{\partial r_{1k}} \frac{\partial r_{1k}}{\partial \mathbf{G}} \\ &+ \frac{\partial \cos\theta_{1jk}}{\partial r_{jk}} \frac{\partial r_{jk}}{\partial \mathbf{G}} \\ &= \left(\frac{1}{r_{1k}} - \frac{\cos\theta_{1jk}}{r_{1j}} \right) \frac{\partial r_{1j}}{\partial \mathbf{G}} + \left(\frac{1}{r_{1j}} - \frac{\cos\theta_{1jk}}{r_{1k}} \right) \frac{\partial r_{1k}}{\partial \mathbf{G}} \\ &- \left(\frac{r_{jk}}{r_{1j}r_{1k}} \right) \frac{\partial r_{jk}}{\partial \mathbf{G}} \end{aligned} \tag{52}$$

According to Eq. (50), $\nabla_X \cdot \mathbf{Q}$ is eventually found as follows,

$$\begin{aligned} \nabla_X \cdot \mathbf{Q} &= \frac{1}{2\Omega_0} \sum_{j=2}^5 \left[\frac{\partial^2 V_{1j}}{\partial r_{1j}^2} \mathbf{R}_{1j} \otimes \mathbf{r}_{1j}^{2nd} + \sum_{k=2}^5 \frac{\partial^2 V_{1j}}{\partial r_{1k}^2} \mathbf{R}_{1k} \otimes \mathbf{r}_{1k}^{2nd} \right. \\ &+ \left\{ \frac{\partial^2 V_{1j}}{\partial \cos\theta_{1jk}^2} \frac{1}{r_{1j}} \left(\frac{1}{r_{1k}} - \frac{\cos\theta_{1jk}}{r_{1j}} \right) \right. \\ &\left. - \frac{\partial V_{1j}}{\partial \cos\theta_{1jk}} \frac{1}{r_{1j}^2} \right\} \mathbf{S}_{1j} \otimes \mathbf{r}_{1j}^{2nd} \\ &+ \left\{ \frac{\partial^2 V_{1j}}{\partial \cos\theta_{1jk}^2} \frac{1}{r_{1k}} \left(\frac{1}{r_{1j}} \right. \right. \\ &\left. \left. - \frac{\cos\theta_{1jk}}{r_{1k}} \right) - \frac{\partial V_{1j}}{\partial \cos\theta_{1jk}} \frac{1}{r_{1k}^2} \right\} \mathbf{S}_{1k} \otimes \mathbf{r}_{1k}^{2nd} \\ &- \left\{ \frac{\partial^2 V_{1j}}{\partial \cos\theta_{1jk}^2} \frac{1}{r_{1j}r_{1k}} \right\} \mathbf{S}_{jk} \otimes \mathbf{r}_{jk}^{2nd} \\ &+ \frac{\partial V_{1j}}{\partial \cos\theta_{1jk}} \frac{1}{r_{1j}} \left(\frac{1}{r_{1k}} - \frac{\cos\theta_{1jk}}{r_{1j}} \right) \mathbf{R}_{1j} \otimes \mathbf{r}_{1j}^{2nd} \\ &+ \frac{\partial V_{1j}}{\partial \cos\theta_{1jk}} \frac{1}{r_{1k}} \left(\frac{1}{r_{1j}} - \frac{\cos\theta_{1jk}}{r_{1k}} \right) \mathbf{R}_{1k} \otimes \mathbf{r}_{1k}^{2nd} \\ &\left. - \frac{\partial V_{1j}}{\partial \cos\theta_{1jk}} \frac{1}{r_{1j}r_{1k}} \mathbf{R}_{jk} \otimes \mathbf{r}_{jk}^{2nd} \right]. \end{aligned} \tag{53}$$

The detailed derivative is somewhat involved, and it can be found in ‘‘Appendix’’. Here we define,

$$\mathbf{r}^{2nd} = \frac{1}{2} \mathbf{G} : (\mathbf{R}_{ij} \otimes \mathbf{R}_{ij}) \tag{54}$$

$$\begin{aligned} S_{mn}^a &= \left(\frac{1}{r_{1k}} - \frac{\cos\theta}{r_{1j}} \right) \frac{r_{1j}^a R_{1j}^a}{r_{1j}} r_{mn}^a \\ &+ \left(\frac{1}{r_{1j}} - \frac{\cos\theta}{r_{1k}} \right) \frac{r_{1k}^a R_{1k}^a}{r_{1k}} r_{mn}^a \\ &- \left(\frac{r_{jk}}{r_{1j}r_{1k}} \right) \frac{r_{jk}^a R_{jk}^a}{r_{jk}} r_{mn}^a. \end{aligned} \tag{55}$$

Moreover the following relations are assumed in the above equations,

$$\begin{aligned} \frac{\partial^2 V_{1j}}{\partial r_{1j}^2} &= \frac{\partial^2 f_C(r_{1j})}{\partial r_{1j}^2} (f_R(r_{1j}) + b_{ij} f_A(r_{1j})) + 2 \frac{\partial f_C(r_{1j})}{\partial r_{1j}} \\ &\left(\frac{\partial f_R(r_{1j})}{\partial r_{1j}} + b_{1j} \frac{\partial f_A(r_{1j})}{\partial r_{1j}} \right) \\ &+ f_C(r_{1j}) \left(\frac{\partial^2 f_R(r_{1j})}{\partial^2 r_{1j}} + b_{1j} \frac{\partial^2 f_A(r_{1j})}{\partial^2 r_{1j}} \right) \end{aligned} \tag{56}$$

$$\begin{aligned} \frac{\partial^2 V_{1j}}{\partial r_{1k}^2} &= f_C(r_{1j}) f_A(r_{1j}) \left\{ \frac{1}{2} \left(\frac{1}{2n} + 1 \right) \right. \\ &\left. (1 + \beta^n \zeta_{1j}^n)^{\frac{-1}{2n} - 2} n \beta^{2n} \zeta_{1j}^{2n-2} \right. \\ &\left. - \frac{1}{2} (n-1) (1 + \beta^n \zeta_{1j}^n)^{\frac{-1}{2n} - 1} \beta^n \zeta_{1j}^{n-2} \right\} \left(\frac{\partial f_C(r_{1k})}{r_{1k}} g(\theta_{1jk}) \right)^2 \\ &+ f_C(r_{1j}) f_A(r_{1j}) \left\{ -\frac{1}{2} (1 + \beta^n \zeta_{1j}^n)^{\frac{-1}{2n} - 1} \beta^n \zeta_{1j}^{n-1} \right\} \\ &\frac{\partial^2 f_C(r_{1k})}{\partial r_{1k}^2} g(\theta_{1jk}) \end{aligned} \tag{57}$$

$$\begin{aligned} \frac{\partial^2 V_{1j}}{\partial \cos\theta_{1jk}^2} &= f_C(r_{1j}) f_A(r_{1j}) \\ &\left\{ \frac{1}{2} \left(\frac{1}{2n} + 1 \right) (1 + \beta^n \zeta_{1j}^n)^{\frac{-1}{2n} - 2} n \beta^{2n} \zeta_{1j}^{2n-2} \right. \\ &\left. - \frac{1}{2} (n-1) (1 + \beta^n \zeta_{1j}^n)^{\frac{-1}{2n} - 1} \beta^n \zeta_{1j}^{n-2} \right\} \frac{\partial \zeta_{1j}}{\partial \cos\theta_{1jk}} \\ &\frac{\partial \zeta_{1j}}{\partial \cos\theta_{1jk}} \end{aligned} \tag{58}$$

$$\begin{aligned} \frac{\partial^2 f_C(r)}{\partial r^2} &= \frac{\pi^2}{4(S-R)^2} \sinh\left(\frac{\pi(r-R)}{2(S-R)}\right) \\ &\cosh^{-3}\left(\frac{\pi(r-R)}{2(S-R)}\right) \end{aligned} \tag{59}$$

2.6 Lennard-Jones potential

In order to evaluate the capacity of the proposed method, we also apply the Lennard-Jones (L-J) potential as a general benchmark potential to solve fracture problems, because of its simplicity. The L-J potential and its derivatives are listed as follows;

$$V^{LJ} = 4\varepsilon \left\{ \left(\frac{\sigma}{r} \right)^{12} - \left(\frac{\sigma}{r} \right)^6 \right\} \tag{60}$$

$$\frac{\partial V^{LJ}}{\partial r} = -\frac{24\varepsilon}{r} \left\{ 2 \left(\frac{\sigma}{r} \right)^{12} - \left(\frac{\sigma}{r} \right)^6 \right\} \tag{61}$$

$$\frac{\partial^2 V^{LJ}}{\partial r^2} = \frac{24\varepsilon}{r^2} \left\{ 26 \left(\frac{\sigma}{r} \right)^{12} - 7 \left(\frac{\sigma}{r} \right)^6 \right\}. \tag{62}$$

Subsequently, we can express stress and higher order stress and its divergence as,

$$\mathbf{P}^{LJ} = \frac{1}{2\Omega_0} \sum_{j=2}^N \frac{\partial V_{1j}^{LJ}}{\partial r_{1j}} \frac{\mathbf{r}_{1j} \otimes \mathbf{R}_{1j}}{r_{1j}} \tag{63}$$

$$\begin{aligned} \mathbf{Q}^{LJ} &= \frac{1}{4\Omega_0} \sum_{j=2}^N \left[\left(\frac{\partial V_{1j}^{LJ}}{\partial r_{1j}} \frac{1}{r_{1j}} \right) \mathbf{r}_{1j} \right. \\ &\left. \otimes \mathbf{R}_{1j} \otimes \mathbf{R}_{1j} \right] \end{aligned} \tag{64}$$

$$\nabla_X \cdot \mathbf{Q}^{LJ} = \frac{1}{2\Omega_0} \sum_{j=2}^N \frac{\partial^2 V_{1j}^{LJ}}{\partial r_{1j}^2} \mathbf{r}_{1j}^{2nd} \otimes \mathbf{R}_{1j}. \tag{65}$$

The parameters, σ and ε for silicon atoms, are taken from [Raghunathan et al. \(2007\)](#), in which the L-J fluid of SiO₂ is studied. For an FCC lattice L-J system, there are twelve first nearest neighbor atoms that are interacting with the central atom at the equilibrium distance.

3 Model evaluation and verification

3.1 Determining of bubble node

An important technical ingredient of the proposed method is how to define the position of the bubble node to represent inhomogeneous deformation in CZ element (see Fig. 3). Here we assume that the degree of the inhomogeneity relates to magnitude of deformation. To do that, a sigmoidal function is introduced to make a correlation between the deformation of CZ element and bubble node position in ζ direction,

$$\zeta_{bub}(t) = \frac{2}{1 + \exp\{-P_{nl}(|\mathbf{F}(t-1) \cdot \mathcal{N}| - 1)\}} - 1, \tag{66}$$

where, ζ_{bub} is the normalized coordinate of bubble node on ζ direction at time t . \mathcal{N} is the normal vector of the CZ element and $\mathbf{F}(t-1)$ is the first order deformation gradient at previous time step. $|\mathbf{F} \cdot \mathcal{N}|$ represents degree of deformation in the direction of cohesive zone element thickness. If deformation gradient \mathbf{F} is unit tensor ζ_{bub} is zero, which means ζ_{bub} locates in the center

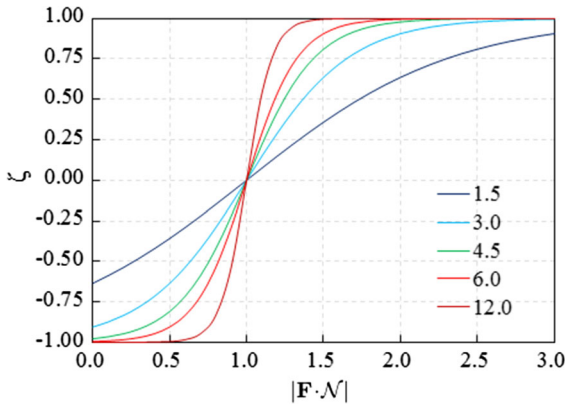


Fig. 6 Relation between deformation and bubble node coordination in ζ direction as a function of the parameter P_{nl} in Eq. (66)

of CZ element (see Fig. 7). Once we can find ζ_{bub} , it is possible to calculate displacement vector \mathbf{d}_{bub} of the bubble node by assuming that $N_7 = 0$ in Eq. (17).

$$\mathbf{d}_{bub} = \sum_{i=1}^6 N_i \left(\xi = \frac{1}{3}, \eta = \frac{1}{3}, \zeta = \zeta_{bub}(t) \right) \mathbf{d}_i. \tag{67}$$

Then, the displacement at the bubble node position is utilized to estimate deformation gradient \mathbf{F} at each Gauss integration point. To simplify the definition, we set $\xi = 1/3$ and $\eta = 1/3$. In Eq. (66), a new adjustable parameter P_{nl} is introduced. Figure 6 visualizes effect of P_{nl} on sensitivity of ζ_{bub} as a function of $|\mathbf{F} \cdot \mathcal{N}|$. ζ_{bub} changes more steeply with increasing P_{nl} . Figure 7 is a schematic drawing of inhomogeneous deformation of the CZ element associated with ζ_{bub} . If $\zeta_{bub} > 0.0$, the CZ element is elongated more at the lower integration points than upper ones, while larger deformation can be seen at upper points when $\zeta_{bub} < 0.0$. In these cases,

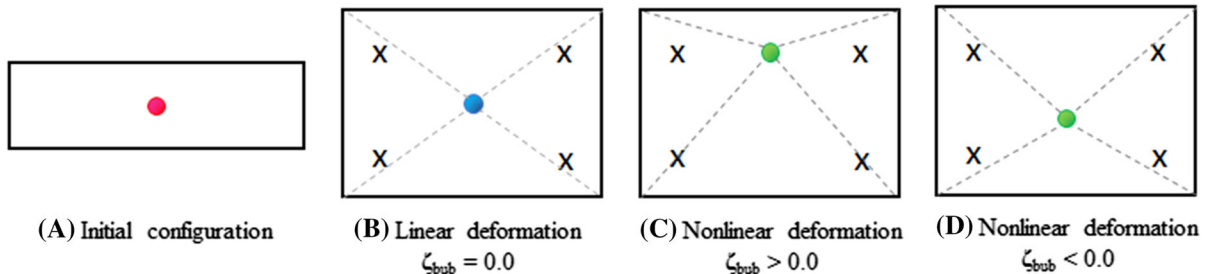


Fig. 7 Schematic drawings of inhomogeneous deformation dependent on bubble node position in the CZ element. Circles and crosses indicate bubble node positions and gauss integration points, respectively

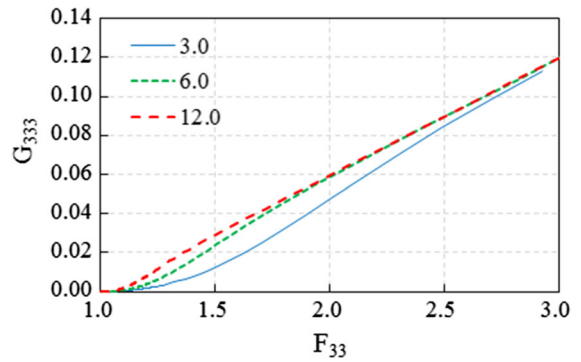


Fig. 8 Gradient of deformation gradient (G_{333}) promoted by heterogeneous deformation of CZ element, when tilted stretch is applied to the model composed of two bulk elements (Fig. 9II). In legend, P_{nl} in Eq. (66) is displayed

different magnitude of stress is emanated at the Gauss integration points due to heterogeneous deformation. Figure 8 shows gradient of deformation gradient G_{333} promoted in CZ element as a function of deformation gradient F_{33} . The gradient is enhanced more when the element is elongated further. The relation can proclaim a hypothesis that effects of initial defects, flaws or any other causes of fracture in material would become evident when material deforms more. It is thus possible to assume that Eq. (66) associates with weakening of fracture process zone when the interface is sufficiently elongated. In addition, we can recognize more heterogeneous deformation is generated by larger P_{nl} even at small deformation range.

3.2 Lennard-Jones potential with FCC lattice

In order to confirm the postulate that the heterogeneous deformation provokes higher fragility of the CZ

Fig. 9 Test models. **I** Antisymmetric uniaxial and **II** tilted stretch of two bulk elements with a cohesive zone element. **III** Cubic specimen composed of 100 bulk elements with 158 cohesive zone elements

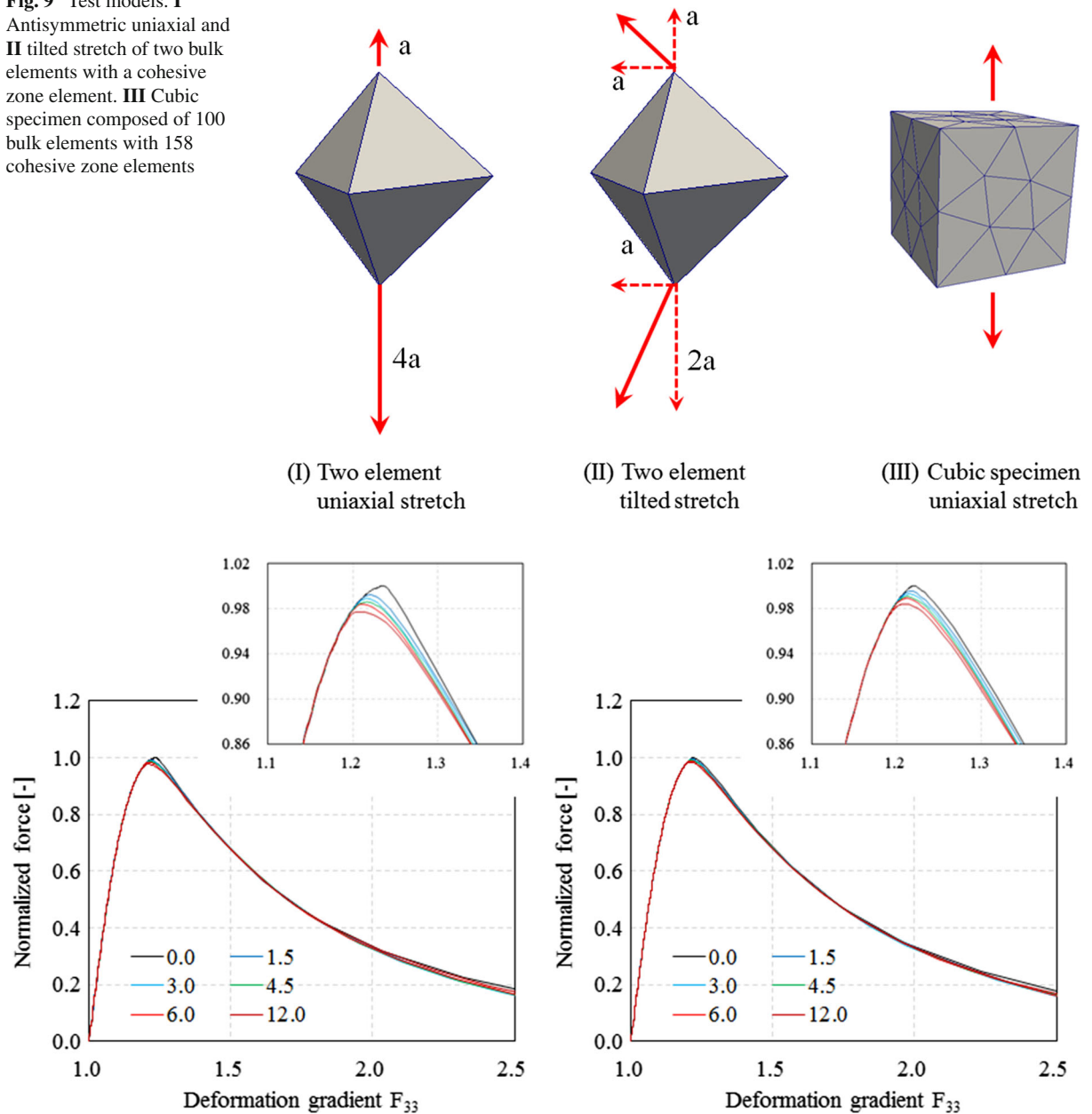


Fig. 10 Effect of bubble node position on weakening of the CZ element by using the L-J potential with FCC lattice. (*Left*) antisymmetric uniaxial stretch and (*right*) tilted stretch of the simplest model composed of two bulk elements. See Fig. 9I, II

element, we employ the simplest model composed of a couple of bulk elements and a CZ element to test hypothesis by using the L-J potential in a crystal with FCC lattice. Antisymmetric uniaxial and tilted stretches are applied to the vertex nodes of the two bulk elements as boundary conditions (Fig. 9I, II). As seen in Fig. 10, the force generated by the CZ element gradu-

ally decreasing with increasing its deformation for both cases. The decline is relatively subtle but the difference is big enough to confine material failure points within the CZ element due to its weakness in strength by being compared with that of the bulk element. Figure 11 shows the effect of second order deformation to decrease the force of CZ element. In this case only

Fig. 11 Effect of 2nd order deformation of force generated in CZ element by using L-J potential with FCC lattice. Tilted stretch of the simplest model composed of two bulk elements are examined

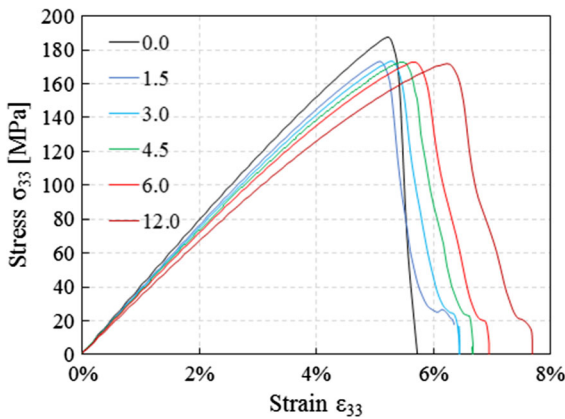
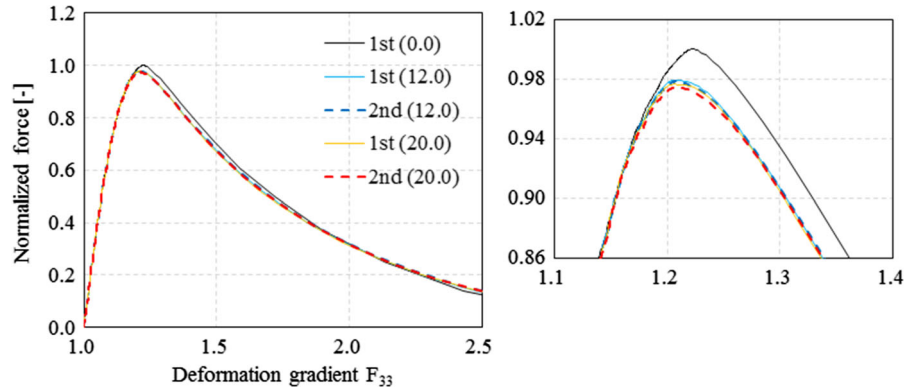


Fig. 12 Stress–strain curve of the cubic specimen with L-J potential (Fig. 9III)

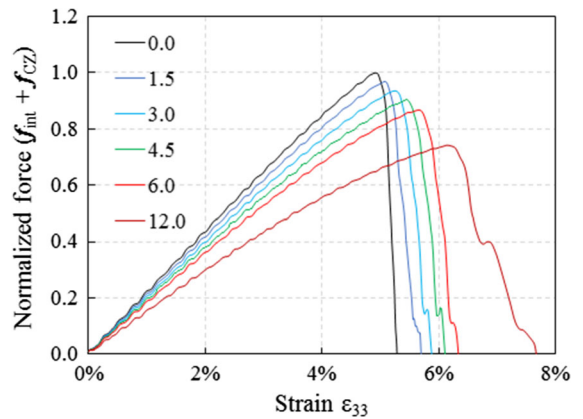


Fig. 13 Relation between strain and total force acting on the bottom face of the cubic specimen by uniaxial stretch with L-J potential

fractional effect is recognized even when we assume relative large P_{nl} . We would discuss the effect by using larger specimen afterward.

Next, a cubic specimen containing multiple CZ elements is studied by using L-J potential with applying uniaxial deformation to vertical direction (Fig. 9III). Figs. 12 and 13 display strain–stress curve and total force evoked on the bottom plane of the specimen, respectively. It is possible to recognize that the elastic constant decreases with increasing the parameter P_{nl} , and the material gets softening monotonically. These results lead a conclusion that the parameter P_{nl} can be rationalized to the CZ element weakening by inhomogeneous deformation as assumed in our definition. If we consider higher order stress \mathbf{Q} associated with second order deformation \mathbf{G} , more fragile condition can be presumed as shown in Fig. 14.

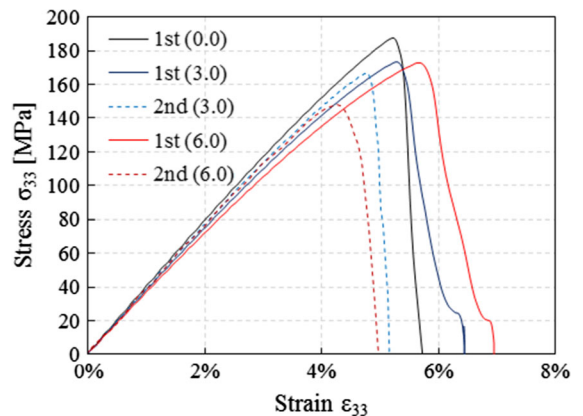


Fig. 14 Effect of second order deformation on the fracture stress of the cubic specimen with L-J potential (Fig. 9III). Parenthesis shows the parameter P_{nl} in Eq. (66)

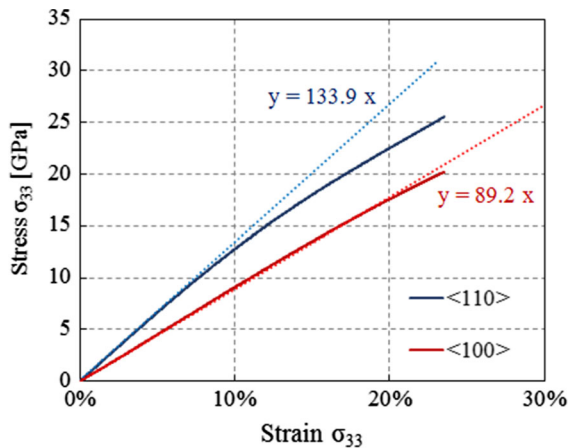


Fig. 15 Strain–stress curve of single-crystal silicon along the $\langle 100 \rangle$ and $\langle 110 \rangle$ directions estimated by Tersoff potential

3.3 Tersoff potential with single-crystal silicon cubic lattice

In this section, we will show the accuracy of single-crystal silicon model that employs the Tersoff potential and diamond cubic lattice (Fig. 5). First, in order to validate the reproducibility of the modulus of single-crystal silicon by using the present method, we have calculated the Young's modulus (E_y) along the $\langle 100 \rangle$ and $\langle 110 \rangle$ directions by using the simplest model composed of two bulk elements and a CZ element (Fig. 9). Figure 15 shows relation between strain and stress generated by symmetric uniaxial stretch. According to the slope at the initial strain region, E_y of $\langle 100 \rangle$ and $\langle 110 \rangle$

are estimated as 89 and 134 GPa, respectively. These values are relatively smaller than experimental values, 130 GPa along the $\langle 100 \rangle$ and 169 GPa for $\langle 110 \rangle$ direction (Hopcroft et al. 2010), however our result is close enough to molecular dynamics simulation at 300K, which estimates Young's modulus along the $\langle 110 \rangle$ is 138 GPa (Kang and Cai 2007). It is thus possible to state that the MCZM using the small unit cell composed of five atoms can reproduce Tersoff's elastic modulus.

Next, we evaluated the fracture stress (σ_f) of silicon in the uniaxial stretch simulation of the cubic specimen (Fig. 9III) with varying parameter P_{nl} . According to Fig. 16, which displays strain–stress curves along the $\langle 100 \rangle$ and $\langle 110 \rangle$ directions, it is obvious that σ_f of the cubic specimen decreases with increasing the parameter P_{nl} , consistently. Therefore, as we inferred, material toughness can be reduced by more heterogeneous deformation in the CZ. To visualize the trend, Fig. 17 summarizes the fracture stress as a function of the parameter P_{nl} , and we can find that the estimated σ_f is from 3.8 to 8.4 GPa. This result is reasonably close to the experimental observations. In Petersen (1982), σ_f of single-crystal silicon is noted as 6.9 GPa. Ericson and Schweitzl have investigated fracture strength of single-crystal silicon by using micron-sized cantilever beams, and reported it is 6.1 ± 0.8 GPa (Ericson and Schweitz 1990). In addition, Li et al. (2005) measured fracture toughness of single-crystal silicon film with and without initial notch, and reported fracture stress of the film without notch is dispersed from 3.6 to 6.4 GPa. One of the possible reasons for such a wide dispersion

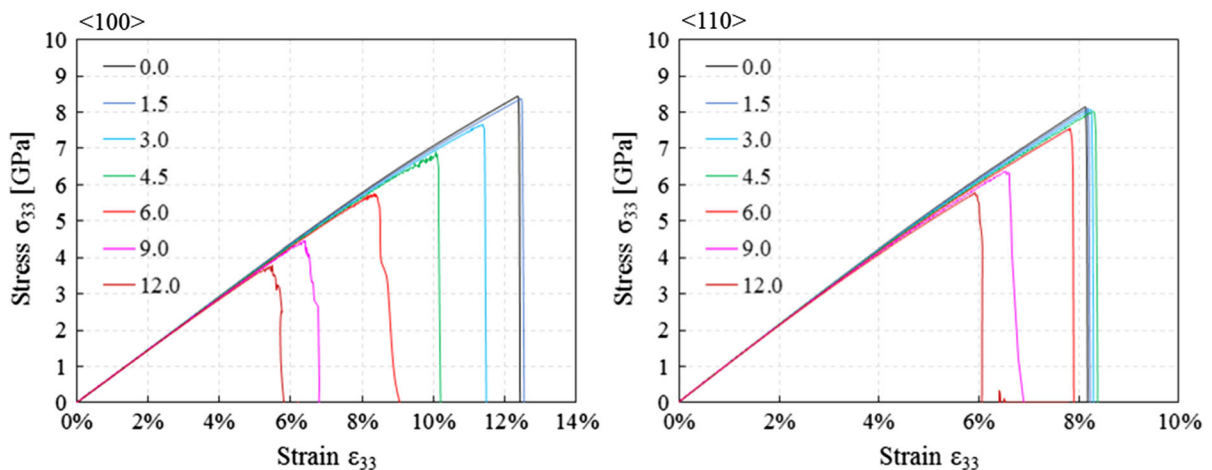


Fig. 16 Strain–stress curve of single-crystal silicon along the $\langle 100 \rangle$ and $\langle 110 \rangle$ directions estimated by the Tersoff potential

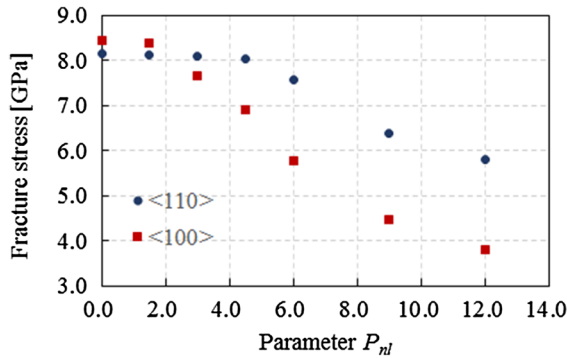


Fig. 17 Shift of the fracture stress of single-crystal silicon by inhomogeneous deformation

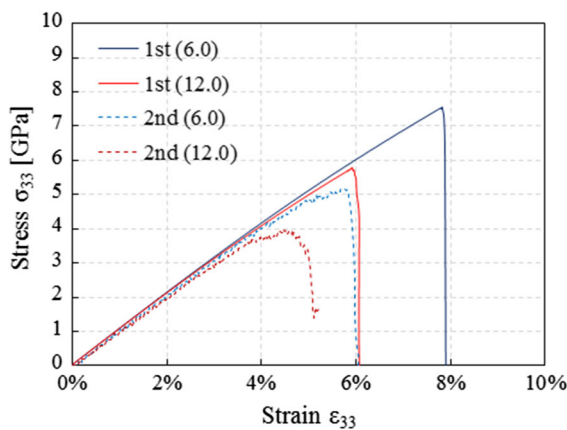


Fig. 18 Simulated fracture stress of single-crystal silicon by considering second order deformation. *Paranthesis* shows the parameter P_{nl} in Eq. (66)

might be initial flaw of the specimen. Analogous to the case of L-J potential, further fragile condition can be assumed with taking second order deformation in CZ as shown in Fig. 18. Interestingly, the adjustable parameter P_{nl} enables us to presume more fragile conditions corresponding to the range experimentally observed. Therefore we conclude that the MCZM can evaluate the fracture stress within reasonable accuracy, although the numerical modeling is not accurate enough. More detailed computational examples are presented in the next section with quantitatively comparison with experimental data.

It is worth noting here that, as discussed in references Kang and Cai (2007) and Hauch et al. (1999), molecular dynamics simulations that are using three body empirical potentials, such as the Tersoff or the Stillinger–Weber (S–W) (Stillinger and Weber 1985) potentials,

cannot estimate fracture stress of single-crystal silicon, because brittle crack propagation does not occur in their simulations. Hauch et al. (1999) have explained that the main reason for this may be related to the short cutoff of these potentials, which induces unreasonable large attraction force before rupture. As a result, MD simulation of silicon nanowire can reach to 30% elongated strain before breaking, and its fracture strength is 26.3 GPa (Kang and Cai 2007), which is obviously larger than the experimental observation. To compensate this shortcoming, Hauch et al. (Hauch et al. (1999)) modified the S–W potential to make the strength of the angle term twice large. It renders brittle fracture, however melting temperature and the Young’s modulus change drastically. Buehler et al. (Buehler et al. (2006)) have shown reactive force field (ReaxFF), which has been developed based on quantum mechanics, is an alternative method to capture crack propagation in silicon, although it is a more expensive interatomic potential. Because the MCZM does not calculate bond rupture intrinsically, it allows us to simulate brittle fracture reasonably, despite of the inevitable drawback of the Tersoff potential.

4 Numerical simulation of fracture toughness

Since it has confirmed that our model is accurate to estimate the essential silicon properties, we apply the method to non-notched and notched microscale silicon film specimens to predict fracture toughness of the thin films, and compare the simulation results with the experimentally measured fracture toughness (Li et al. 2005; Nakao et al. 2008; Ando et al. 2005; Wong and Holbrook 1987). In Fig. 19, the dimension of a single-edge-notched tension specimen is illustrated.

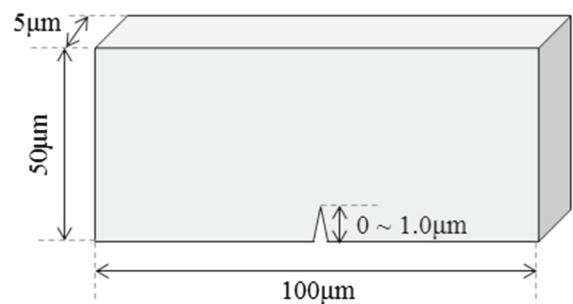
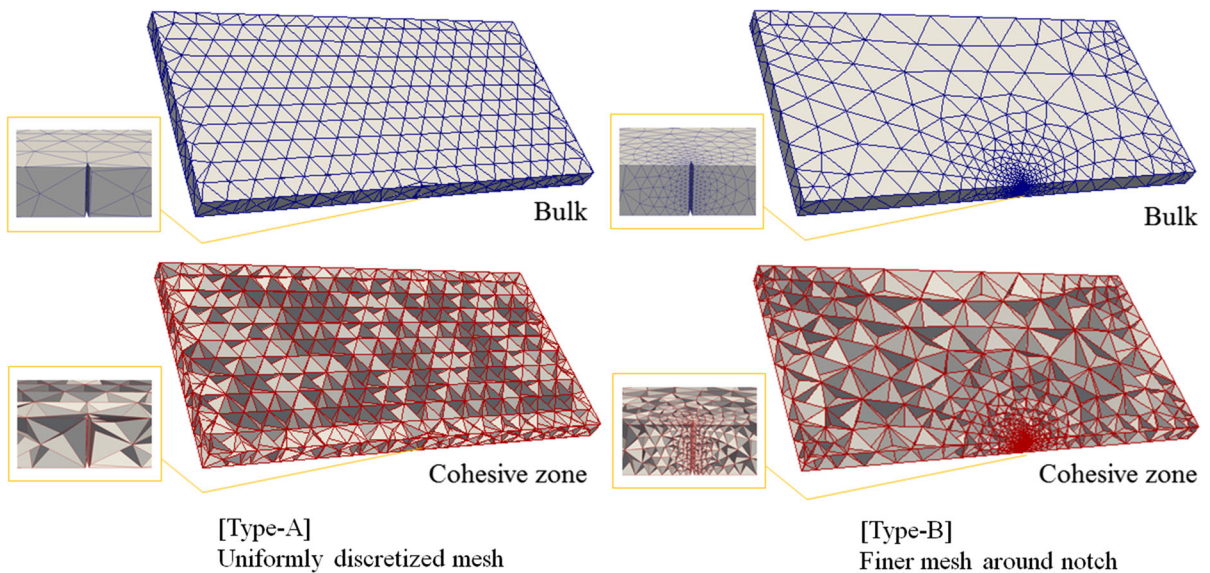


Fig. 19 Size of thin specimen used to calculate the fracture stress of single-crystal silicon

Table 1 Mesh size of 1.0 μm notched specimen examined by using the Lennard-Jones potential

	Mesh A (1)			Mesh A (2)		Mesh A (3)	Mesh B
Node	2612			9132		52,836	11,664
Bulk element	653			2283		13,209	2916
CZ element	1143			3963		23,866	5192
Total element	1796			6246		37,075	8108
Avg. element vol. (μm^3)	38.28			10.95		1.89	8.57
Avg. side length (μm)	4.8			3.1		1.7	2.9
CZ thickness p_{th} (—)	0.02	0.013	0.007	0.02	0.013	0.02	0.01
Avg. CZ thickness (μm)	0.095	0.063	0.035	0.063	0.035	0.035	0.029

**Fig. 20** Two types of mesh discretization. (*Left*) uniform size (*right*) Finer mesh around notch

4.1 Simulation condition test

At first, we examine sensitivities of mesh patterns, mesh size, and CZ thickness for fracture stress estimation by using the L-J potential. The notch length of the specimen was designed as 1.0 μm . The detail of model is summarized in Table 1. We prepared two types of FEM discretizations: one is composed of relatively uniform size of elements (Type-A), and another has finer meshes around the notch (Type-B), as drawn in Fig. 20. For the Type-A mesh, three different density of meshes were investigated.

Because the thickness of CZ element depends on the element size according to Eq. (20), we examined different size of CZ thickness, such as 0.035,

0.063 and 0.095 μm in average, by adjusting parameter p_{th} . In this simulation, time interval was set to 1.0×10^{-4} ns, and constant displacement boundary condition of 5×10^4 m/s was applied to the both side edges of the specimen. The total integration time until material fracture was about 300–400 ns. All these test calculations were carried out by using the first order Cauchy–Born rule with linear CZ element ($P_{nt} = 0$).

The computationally estimated fracture stress σ_f is shown in Table 2, and crack patterns are visually illustrated in Figs. 21 and 22. According to these results for Type-A meshes, the fracture pattern and σ_f are sensitive to mesh size but not much to CZ element thickness. In the case of the coarse Mesh (A-1), only the model with the thinnest cohesive zone width shows the

Table 2 Results of the calculations of fracture stress of the noted specimen (1.0 μm) by using the Lennard-Jones potential

	CZ thickness		Fracture stress	
	p_{th} (-)	Avg. (μm)	σ_f (MPa)	Ratio with Mesh A (3)
Mesh A (1)	0.020	0.095	142	158 %
	0.013	0.063	129	144 %
	0.007	0.035	134	149 %
Mesh A (2)	0.020	0.063	110	122 %
	0.011	0.035	100	111 %
Mesh A (3)	0.020	0.035	90	–
Mesh B	0.010	0.029	59	66 %

Fig. 21 Crack path of the specimen with 1.0 [μm] initial notch calculated by using the Lennard-Jones potential to check calculation conditions. Mesh Type-A. Parenthesis indicates average thickness of cohesive zone element

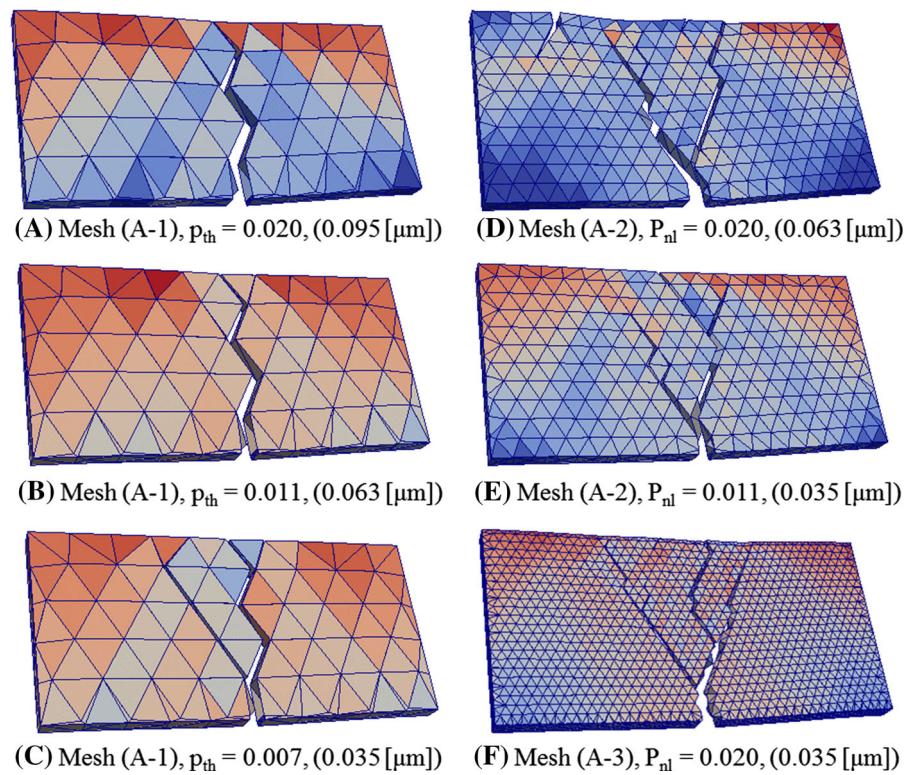
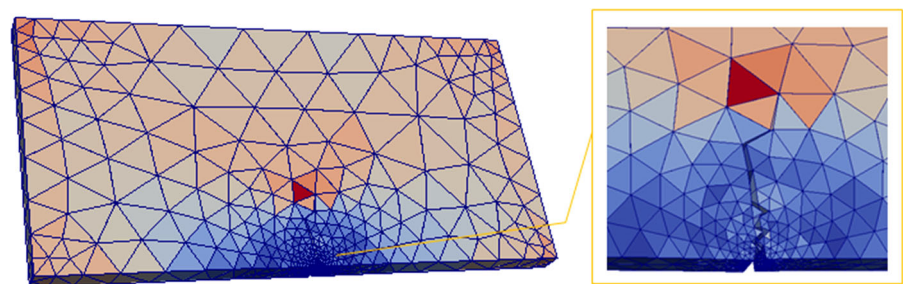


Fig. 22 Crack initiated in the specimen with 1.0 [μm] initial notch calculated by using the Lennard-Jones potential. Mesh Type-B



branched crack path that is analogous to the case of the finer meshes. However, even for the case with the thinnest cohesive zone width, $p_{th} = 0.007$, σ_f is about 50 % larger than that of the finest Mesh (A-3). On the other hand, Mesh (A-2) can reproduce σ_f with only 11 % difference from that of the Mesh (A-3), if the cohesive zone thickness has the same value. Additionally, both cases of two different CZ thickness of Mesh (A-2) show branched crack paths. Therefore, we find that Mesh (A-2) is sufficiently appropriate enough to examine fracture in the notched specimen. Of course, Mesh (A-3) can demonstrate more realistic crack path and reliable fracture properties, however, it may be too expensive in simulation by using with the Tersoff potential. This is because that the potential requires three body interaction, and in each time step we need to optimize internal displacement vector \mathbf{v} by using the Newton-Raphson iteration method.

In contrary, the Type-B mesh shows obviously lower toughness being compared with that of Type-A. Finer mesh around the notch might be able to reproduce more precise stress distribution, and this may be attributed to crack initiation at smaller strain. We therefore examine Type-A(2) mesh and Mesh B to measure fracture toughness of the single-crystal silicon with the Tersoff potential.

4.2 Fracture toughness of single-crystal silicon

For the single-crystal silicon simulation, the simulation time interval is set to 1.0×10^{-4} ns, and uniaxial stretch is at the rate 3×10^5 m/s in horizontal direction was applied. The crystal orientation in stretched direction is $\langle 110 \rangle$.

First, non-notched specimen was examined with a model discretized by comparable mesh size with Mesh A(2) for $1.0 \mu\text{m}$ notched specimen. The detail of model and simulation results are elaborated in Table 3. The non-notched specimen was cracked at 5.7 and 4.9 GPa stress for $P_{nl} = 0.0$ (liner) and 9.0, respectively. These results are analogous to the case of small cubic specimen which is investigated in Sect. 3.3. Fracture stress of single-crystal silicon is reported as 6.9 [see Petersen (1982)] and 6.1 ± 0.8 GPa [see Ericson and Schweitz (1990)]. Li et al. Li et al. (2005) measured fracture stress of the micron size silicon film and it is from 3.0 to 6.4 GPa. It is therefore reasonable to say that the proposed method can predict the fracture stress by adjusting the empirical parameter P_{nl} in a reasonable

Table 3 Model and simulation results of fracture stress for non-notched specimen of single-crystal silicon by using the Tersoff potential

Mesh model	
Node	9348
Bulk element	2337
CZ element	4074
Total element	6411
CZ thickness $p_{th}(-)$	0.011
Simulation result of the fracture stress σ_f (GPa)	
$P_{nl} = 0.0$ (linear)	5.7
$P_{nl} = 9.0$	4.9

range associated with experimental error for the testing specimen.

Next, a numerical simulation of crack growth in a specimen with a notch was performed, in which the initial notch length is $1.0 \mu\text{m}$. For the single-edge-notched specimen, fracture toughness K_{IC} is evaluated by measuring the fracture stress σ_f according to the following equation (Nakao et al. 2008),

$$K_{IC} = Y\sigma_f\sqrt{\pi a}, \quad (68)$$

where a is the notch length, and the parameter Y is calculated based the following formula,

$$Y = 1.12 - 0.231\lambda + 10.55\lambda^2 - 21.72\lambda^3 + 30.39\lambda^4, \quad (69)$$

where, λ is ratio of notch length and specimen width as $\lambda = a/W$. Experimentally observed K_{IC} of single-crystal silicon is in the range of 0.82–1.0 MPa m^{1/2} as summarized in Wong and Holbrook (1987). For the micron scale single-edge-notched specimen, slightly higher values are reported, e.g. 1.28 MPa m^{1/2} (Nakao et al. 2008), 1.13–1.74 MPa m^{1/2} (Ando et al. 2005), by loading to $\langle 110 \rangle$ direction. The range of these experimentally estimated K_{IC} corresponds to fracture stress from 0.41 to 0.88 GPa, according to Eq. (68). Fracture stress of the $1.0 \mu\text{m}$ single-edge-notched $100 \mu\text{m}$ width specimen was also reported as 0.85 GPa (Li et al. 2005).

The simulated fracture stress of the single-notched specimen are listed in Table 4. In the case of Mesh A(2), assuming uniform deformation in CZ element ($P_{nl} = 0$), crack cannot be initiated from the notch until 3.0 GPa tensile stress is reached, and eventually the specimen was broken from the edge. Applying non-

Table 4 Calculated yield toughness of 1.0 μm notched single-crystal silicon specimen by using Tersoff potential. Loading direction is $\langle 110 \rangle$. Parenthesis indicates order of Cauchy–Born rule considered

	CZ thickness		P_{nl} for CZ	Fracture stress	Fracture toughness
	p_{th} (–)	Avg. (μm)	P_{nl} (–)	σ_y (GPa)	K_{IC} (MPa $\text{m}^{1/2}$)
Mesh A (2)	0.011	0.035	0.0 (1st)	3.0	6.0
			9.0 (1st)	2.7	5.4
Mesh B	0.010	0.029	0.0 (1st)	2.3	4.6
			12.0 (1st)	2.1	4.2
			36.0 (1st)	1.5	3.0
			36.0 (2nd)	1.4	2.8
			60.0 (1st)	1.5	3.0
			60.0 (2nd)	1.2	2.4

linear deformation for CZ with $P_{nl} = 9.0$ makes the specimen weaker only slightly and the specimen is torn from the notch at 2.7 GPa. The fracture stress is still not comparable to the experimental data. It is thus obvious, Mesh A(2), which equally discretizes the specimen, overestimates the fracture toughness.

Even for Mesh (B), which is discretized with finer mesh around the notch, the estimated fracture stress is much higher than experimental data until $P_{nl} = 36.0$. We need to set a very high heterogeneous deformation in CZ with $P_{nl} = 60.0$ to obtain the second order stress effect on the fracture stress that conforms to experimentally measured fracture stress of the notched specimen. The experimental fracture stress corresponds to about 1.0% strain. Therefore, the presumable reason would be because crack should be initiated at such extremely small deformation. Since our method associates nonuniform deformation in CZ with deformation tensor \mathbf{F} , heterogeneous deformation can be provoked at such small deformation only by sufficiently large P_{nl} .

According to these results, it is reasonable to conclude that we can use MCZM with the Tersoff potential to predict the fracture stress quantitatively in comparison with experimental observations, although the parameter P_{nl} that represents nonuniform deformation in CZ, should be adjusted to the system studied.

5 Conclusions

In order to simulate fracture and crack propagation in single-crystal silicon films, we modified and extended the Multiscale Cohesive Zone Method (MCZM) to three-dimensional case for crystals with non-Bravais lattice. The multiscale constitutive models in both bulk crystal as well as fracture process zone are derived

based on the Cauchy–Born rules from the tetrahedral Si–Si₄ lattice unit cell that is embedded at every quadrature points.

In this study, instead of using the so-called depletion potential, we adopt a higher order Cauchy–Born rule approach to take account of strain gradient effect in constitutive modeling. The key for a successful simulation of fracture is that we use different order of the Cauchy–Born rules in the bulk element and the cohesive element respectively, which provides a natural failure selection as the failure thresholds in different elements will be different if the order of the Cauchy–Born rule used is different. Since material failure, or fracture in this case, often occurs first at where the deformation is inhomogeneous, therefore the higher order Cauchy–Born rule governed cohesive zone will always fracture first and it hence forms a crack path.

In doing so, we utilize the wedge element with an bubble node to capture the non-uniform deformation in cohesive elements, which represents inherent weakness of cohesive zone. For this purpose, we conceived a new numerical scheme to make the inhomogeneous deformation at each gauss integration points by using only first order deformation tensor \mathbf{F} . In addition, we have introduced a sigmoidal function to make relation between degree of inhomogeneous deformation and bubble node position.

Moreover, the single-crystal Si–Si₄ is not a Bravais lattice, and it has an internal vector to form a diamond cubic lattice. We employed the modified Cauchy–Born rule for the non-Bravais lattice in deriving the macroscale stress-strain relation with the Tersoff potential for the single-crystal Si–Si₄ lattices. Note that this modified Cauchy–Born is implemented in both the first order Cauchy–Born rule as well as the second order Cauchy–Born rule.

Numerical examinations by using relatively small scale models with the Lennard-Jones and the Tersoff potentials have shown that it is possible to reduce the toughness of CZ element compared with bulk element by using only an empirical parameter to define the position of the bubble node in CZ element. This assumption maintains linear deformation when the deformation of CZ element is small enough, while heterogeneity degree increases with increasing the CZ deformation. If we apply the MCZM to more complex crystals or amorphous materials, more atoms in a unit cell are necessary to calculate stress-strain relation. By comparing with Molecular Dynamics simulation, MCZM is a much economical option, because a Molecular Dynamics simulation system of $100\ \mu\text{m} \times 50\ \mu\text{m} \times 5\ \mu\text{m}$ film would contain more than trillions of atoms ($>10^{13}$), with even today's fastest computer, it would take a long time and considerable resource to perform such simulations. For instance, it takes over a day to simulate stretch of only $13\ \text{nm} \times 13\ \text{nm} \times 13\ \text{nm}$ size of single-crystal silicon by using the sophisticated MD code, LAMMPS (Plimpton 1995), with eight cores parallel computing. On the other hand, only about an hour is sufficient to compute the fracture stress of single-crystal silicon with cubic specimen (Fig. 9III) by using a single core desktop computer. It is thus prohibitively expensive to simulate material fracture for such large and complex systems with atomistic resolution. Therefore, the method proposed in this study is useful to contain increasing of computational cost of MD simulation, and to offer a simple simulation model for the practical applications.

After examining sensitivities of mesh size and CZ element thickness, we demonstrated 3D simulations of fracture of non-notched and notched thin single-crystal silicon films. The simulated fracture stress of non-notched specimen was 5.7 GPa, and it quantitatively agrees with the experimental data. In addition, it was demonstrated that more general condition may be assumed if non-uniform deformation was assigned by an adjustable parameter P_{nl} . In the case of $1.0\ \mu\text{m}$ single-edge-notched specimen, relatively larger P_{nl} was indispensable to reproduce experimental fracture toughness. This is because crack is initiated at small deformation in the notched specimen.

Acknowledgements Dr. S. Urata is sponsored by Asahi Glass Co., Ltd. Japan, and this support is greatly appreciated. The

authors gratefully acknowledge helpful discussions with Ms. D. Lyu and Dr. H. Fan.

Appendix

Appendix 1: Optimization of inner vector of diamond cubic lattice

First, we document the procedure on how to find the inner vector \mathbf{v} position based on strain energy minimization.

In order to satisfy Eq. (40), we use Newton's method,

$$\mathbf{v}^{i+1} = \mathbf{v}^i + \delta\mathbf{v} \quad (70)$$

$$\delta\mathbf{v} = \left(\frac{\partial^2 V}{\partial \mathbf{v}^2}\right)^{-1} \left(\frac{\partial V}{\partial \mathbf{v}}\right). \quad (71)$$

Then, similar to Eq. (41), one may find that

$$\begin{aligned} \frac{\partial V}{\partial \mathbf{v}} &= \frac{1}{2\Omega_0} \sum_{j=2}^5 \left(\frac{\partial V_{1j}}{\partial \mathbf{v}}\right) \\ &= \frac{1}{2\Omega_0} \sum_{j=2}^5 \left[\frac{\partial V_{1j}}{\partial r_{1j}} \frac{\partial r_{1j}}{\partial \mathbf{v}} \right. \\ &\quad \left. + \sum_{k=2, j \neq k}^5 \left(\frac{\partial V_{1j}}{\partial r_{1k}} \frac{\partial r_{1k}}{\partial \mathbf{v}} + \frac{\partial V_{1j}}{\partial \cos\theta_{1jk}} \frac{\partial \cos\theta_{1jk}}{\partial \mathbf{v}} \right) \right] \end{aligned} \quad (72)$$

where

$$\begin{aligned} \frac{\partial \cos\theta_{1jk}}{\partial \mathbf{v}} &= \frac{\partial r_{1j}}{\partial \mathbf{v}} \frac{\partial \cos\theta_{1jk}}{\partial r_{1j}} + \frac{\partial r_{1k}}{\partial \mathbf{v}} \frac{\partial \cos\theta_{1jk}}{\partial r_{1k}} \\ &\quad + \frac{\partial r_{jk}}{\partial \mathbf{v}} \frac{\partial \cos\theta_{1jk}}{\partial r_{jk}} \\ &= \left(\frac{1}{r_{1k}} - \frac{\cos\theta_{1jk}}{r_{1j}}\right) \frac{\partial r_{1j}}{\partial \mathbf{v}} + \left(\frac{1}{r_{1j}} - \frac{\cos\theta_{1jk}}{r_{1k}}\right) \frac{\partial r_{1k}}{\partial \mathbf{v}} \\ &\quad - \left(\frac{r_{jk}}{r_{1j}r_{1k}}\right) \frac{\partial r_{jk}}{\partial \mathbf{v}} \end{aligned} \quad (73)$$

and

$$\frac{\partial r_{ij}}{\partial \mathbf{v}} = \begin{cases} \frac{\partial r_{1j}}{\partial \mathbf{v}} \frac{\partial \mathbf{r}_{1j}}{\partial \mathbf{v}} = -\frac{\mathbf{r}_{1j}}{r_{1j}} & i, j \in \alpha, \text{ or } i, j \in \beta \\ 0 & \text{otherwise} \end{cases} \quad (74)$$

For the second derivative,

$$\frac{\partial^2 V}{\partial \mathbf{v}^2} = \frac{1}{2\Omega_0} \sum_{j=2}^5 \left(\frac{\partial^2 V_{1j}}{\partial \mathbf{v}^2}\right)$$

$$\begin{aligned}
&= \frac{1}{2\Omega_0} \sum_{j=2}^5 \left[\frac{\partial^2 V_{1j}}{\partial r_{1j}^2} \frac{\partial r_{1j}}{\partial \mathbf{v}} \frac{\partial r_{1j}}{\partial \mathbf{v}} + \frac{\partial V_{1j}}{\partial r_{1j}} \frac{\partial^2 r_{1j}}{\partial \mathbf{v}^2} \right. \\
&+ \sum_{k=2, j \neq k}^5 \left\{ \frac{\partial V_{1j}^2}{\partial r_{1k}^2} \frac{\partial r_{1k}}{\partial \mathbf{v}} \frac{\partial r_{1k}}{\partial \mathbf{v}} + \frac{\partial V_{1j}}{\partial r_{1k}} \frac{\partial^2 r_{1k}}{\partial \mathbf{v}^2} \right. \\
&\left. \left. + \frac{\partial V_{1j}^2}{\partial \cos\theta_{1jk}^2} \frac{\partial \cos\theta_{1jk}}{\partial \mathbf{v}} \frac{\partial \cos\theta_{1jk}}{\partial \mathbf{v}} + \frac{\partial V_{1j}}{\partial \cos\theta_{1jk}} \frac{\partial^2 \cos\theta_{1jk}}{\partial \mathbf{v}^2} \right\} \right] \quad (75)
\end{aligned}$$

$$\begin{aligned}
\frac{\partial^2 \cos\theta_{1jk}}{\partial \mathbf{v}^2} &= \left(\frac{1}{r_{1k}} - \frac{\cos\theta_{1jk}}{r_{1j}} \right) \frac{\partial^2 r_{1j}}{\partial \mathbf{v}^2} + \left(\frac{1}{r_{1j}} - \frac{\cos\theta_{1jk}}{r_{1k}} \right) \frac{\partial^2 r_{1k}}{\partial \mathbf{v}^2} \\
&+ \left(-\frac{1}{r_{1k}^2} \frac{\partial r_{1k}}{\partial \mathbf{v}} - \frac{\partial \cos\theta_{1jk}}{\partial \mathbf{v}} \frac{1}{r_{1j}} + \frac{\cos\theta_{1jk}}{r_{1j}^2} \frac{\partial r_{1j}}{\partial \mathbf{v}} \right) \frac{\partial r_{1j}}{\partial \mathbf{v}} \\
&+ \left(-\frac{1}{r_{1j}^2} \frac{\partial r_{1j}}{\partial \mathbf{v}} - \frac{\partial \cos\theta_{1jk}}{\partial \mathbf{v}} \frac{1}{r_{1k}} + \frac{\cos\theta_{1jk}}{r_{1k}^2} \frac{\partial r_{1k}}{\partial \mathbf{v}} \right) \frac{\partial r_{1k}}{\partial \mathbf{v}} \quad (76)
\end{aligned}$$

where the following relation,

$$\frac{\partial^2 r_{ij}}{\partial \mathbf{v}^2} = \begin{cases} \frac{\partial}{\partial \mathbf{v}} \left(-\frac{\mathbf{r}_{ij}}{r_{ij}} \right) = \frac{1}{r_{ij}} \left(\mathbf{I} - \frac{\mathbf{r}_{ij} \mathbf{r}_{ij}}{r_{ij}^2} \right), & i, j \in \alpha \text{ or } i, j \in \beta \\ 0, & \text{otherwise} \end{cases} \quad (77)$$

and Eqs. (56)–(59) are applied.

Appendix 2: Divergence of the second order stress tensor

Second, we show how to find the divergence of the second order stress tensor based on the higher Cauchy–Born rule for the Tersoff potential.

According to Eqs. (50)–(53), we have,

$$\begin{aligned}
\nabla_X \cdot \mathbf{Q} &= \frac{1}{2\Omega_0} \sum_{j=2}^5 \left[\nabla_X \left(\frac{\partial V_{1j}}{\partial r_{1j}} \frac{1}{2r_{1j}} \right) \mathbf{r}_{1j} \otimes \mathbf{R}_{1j} \otimes \mathbf{R}_{1j} \right. \\
&+ \left(\frac{\partial V_{1j}}{\partial r_{1j}} \frac{1}{2r_{1j}} \right) \nabla_X \cdot (\mathbf{r}_{1j} \otimes \mathbf{R}_{1j} \otimes \mathbf{R}_{1j}) \\
&+ \sum_{k=2, k \neq j}^5 \left[\nabla_X \left(\frac{\partial V_{1j}}{\partial r_{1k}} \frac{1}{2r_{1k}} \right) \mathbf{r}_{1k} \otimes \mathbf{R}_{1k} \otimes \mathbf{R}_{1k} \right. \\
&+ \left(\frac{\partial V_{1j}}{\partial r_{1k}} \frac{1}{2r_{1k}} \right) \nabla_X \cdot (\mathbf{r}_{1k} \otimes \mathbf{R}_{1k} \otimes \mathbf{R}_{1k}) \\
&+ \nabla_X \left\{ \left(\frac{\partial V_{1j}}{\partial \cos\theta} \frac{1}{2r_{1j}} \right) \left(\frac{1}{r_{1k}} - \frac{\cos\theta}{r_{1j}} \right) \right\} \mathbf{r}_{1j} \otimes \mathbf{R}_{1j} \otimes \mathbf{R}_{1j} \\
&+ \left\{ \left(\frac{\partial V_{1j}}{\partial \cos\theta} \frac{1}{2r_{1j}} \right) \left(\frac{1}{r_{1k}} - \frac{\cos\theta}{r_{1j}} \right) \right\} \nabla_X \cdot (\mathbf{r}_{1j} \otimes \mathbf{R}_{1j} \otimes \mathbf{R}_{1j}) \\
&+ \nabla_X \left\{ \frac{\partial V_{1j}}{\partial \cos\theta} \frac{1}{2r_{1k}} \left(\frac{1}{r_{1j}} - \frac{\cos\theta}{r_{1k}} \right) \right\} \mathbf{r}_{1k} \otimes \mathbf{R}_{1k} \otimes \mathbf{R}_{1k} \\
&+ \left\{ \frac{\partial V_{1j}}{\partial \cos\theta} \frac{1}{2r_{1k}} \left(\frac{1}{r_{1j}} - \frac{\cos\theta}{r_{1k}} \right) \right\} \nabla_X \cdot (\mathbf{r}_{1k} \otimes \mathbf{R}_{1k} \otimes \mathbf{R}_{1k}) \right]
\end{aligned}$$

$$\begin{aligned}
&- \nabla_X \left\{ \frac{\partial V_{1j}}{\partial \cos\theta} \frac{1}{2r_{jk}} \left(\frac{r_{jk}}{r_{1j} r_{1k}} \right) \right\} \mathbf{r}_{jk} \otimes \mathbf{R}_{jk} \otimes \mathbf{R}_{jk} \\
&- \left\{ \frac{\partial V_{1j}}{\partial \cos\theta} \frac{1}{2r_{jk}} \left(\frac{r_{jk}}{r_{1j} r_{1k}} \right) \right\} \nabla_X \cdot (\mathbf{r}_{jk} \otimes \mathbf{R}_{jk} \otimes \mathbf{R}_{jk}) \right] \quad (78)
\end{aligned}$$

and based on the above equation, we can write the following expressions with abbreviating index,

$$\begin{aligned}
&\nabla_X \left(\frac{\partial V}{\partial r} \frac{1}{2r} \right) \mathbf{r} \otimes \mathbf{R} \otimes \mathbf{R} + \left(\frac{\partial V}{\partial r} \frac{1}{2r} \right) \nabla_X \cdot (\mathbf{r} \otimes \mathbf{R} \otimes \mathbf{R}) \\
&= \left[\frac{\partial}{\partial X_C} \left(\frac{\partial V}{\partial r} \frac{1}{2r} \right) + \left(\frac{\partial V}{\partial r} \frac{1}{2r} \right) \frac{\partial}{\partial X_C} \right] r_a R_A R_B (\mathbf{e}_a \otimes \mathbf{E}_A \otimes \mathbf{E}_B) \cdot \mathbf{E}_C \\
&= \left[\frac{\partial}{\partial r} \frac{\partial r}{\partial F} \frac{\partial F}{\partial X_B} \left(\frac{\partial V}{\partial r} \frac{1}{2r} \right) + \left(\frac{\partial V}{\partial r} \frac{1}{2r} \right) \frac{\partial}{\partial r} \frac{\partial r}{\partial F} \frac{\partial F}{\partial X_B} \right] r_a R_A R_B (\mathbf{e}_a \otimes \mathbf{E}_A) \\
&= \frac{1}{2} \frac{\partial^2 V}{\partial r^2} R_a G_B R_A R_B = \frac{\partial^2 V}{\partial r^2} \mathbf{R} \otimes \mathbf{r}^{2nd} \quad (79)
\end{aligned}$$

Here, \mathbf{r}^{2nd} is the additional term in atom coordination [see Eq. (27)] owing to second order deformation. And, an example for the angle term is,

$$\begin{aligned}
&\nabla_X \left[\left(\frac{\partial V_{1j}}{\partial \cos\theta} \frac{1}{2r_{1j}} \right) \left(\frac{1}{r_{1k}} - \frac{\cos\theta}{r_{1j}} \right) \right] \mathbf{r}_{1j} \otimes \mathbf{R}_{1j} \otimes \mathbf{R}_{1j} \\
&= \frac{\partial}{\partial \cos\theta} \left[\left(\frac{\partial V_{1j}}{\partial \cos\theta} \frac{1}{2r_{1j}} \right) \left(\frac{1}{r_{1k}} - \frac{\cos\theta}{r_{1j}} \right) \right] \\
&\quad \times \frac{\partial \cos\theta}{\partial F} \frac{\partial F}{\partial X_B} r_{1j}^a R_{1j}^A R_{1j}^B (\mathbf{e}_a \otimes \mathbf{E}_A) \\
&= \left[\left(\frac{\partial^2 V_{1j}}{\partial \cos^2 \theta} \frac{1}{2r_{1j}} \right) \left(\frac{1}{r_{1k}} - \frac{\cos\theta}{r_{1j}} \right) - \left(\frac{\partial V_{1j}}{\partial \cos\theta} \frac{1}{2r_{1j}} \right) \frac{1}{r_{1j}} \right] \\
&\quad \frac{\partial \cos\theta}{\partial F} G_B r_{1j}^a R_{1j}^A R_{1j}^B (\mathbf{e}_a \otimes \mathbf{E}_A), \quad (80)
\end{aligned}$$

where $\partial \cos\theta / \partial \mathbf{F}$ has shown in Eq. (43), and

$$\begin{aligned}
&\frac{\partial V_{1j}}{\partial \cos\theta} \frac{1}{2r_{1j}} \left(\frac{1}{r_{1k}} - \frac{\cos\theta}{r_{1j}} \right) \nabla_X \cdot (\mathbf{r}_{1j} \otimes \mathbf{R}_{1j} \otimes \mathbf{R}_{1j}) \\
&= \frac{\partial V_{1j}}{\partial \cos\theta} \frac{1}{2r_{1j}} \left(\frac{1}{r_{1k}} - \frac{\cos\theta}{r_{1j}} \right) \frac{\partial}{\partial r} \frac{\partial r}{\partial F} \frac{\partial F}{\partial X_B} r_{1j}^a R_{1j}^A R_{1j}^B (\mathbf{e}_a \otimes \mathbf{E}_A) \\
&= \frac{\partial V_{1j}}{\partial \cos\theta} \frac{1}{2r_{1j}} \left(\frac{1}{r_{1k}} - \frac{\cos\theta}{r_{1j}} \right) \frac{r_{1j}^a R_{1j}^A r_{1j}^B}{r_{1j}} G_B R_{1j}^A R_{1j}^B (\mathbf{e}_a \otimes \mathbf{E}_A) \\
&= \frac{\partial V_{1j}}{\partial \cos\theta} \frac{1}{r_{1j}} \left(\frac{1}{r_{1k}} - \frac{\cos\theta}{r_{1j}} \right) \mathbf{R}_{1j} \otimes \mathbf{r}_{1j}^{2nd}. \quad (81)
\end{aligned}$$

Appendix 3: Second order shape function with a bubble mode

Second order shape function for wedge element with a bubble node in the center of element. Node positions are illustrated in Fig. 23.

$$N_1 = -\frac{1}{2} (1 - \xi - \eta) (2\xi + 2\eta + \zeta) (1 - \zeta) - \frac{1}{15} N_{16}$$

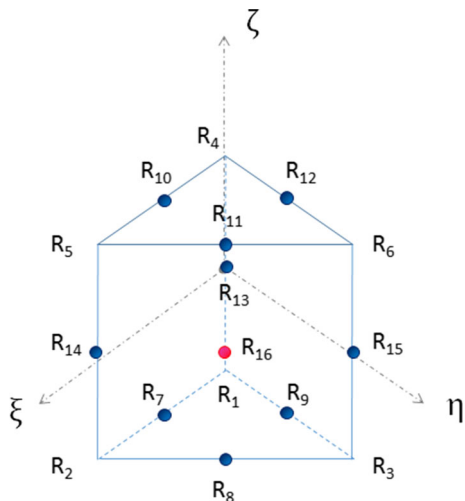


Fig. 23 Fifteen nodes of isoparametric triangular prism element and a bubble node. Red circle is the point of a bubble node

$$\begin{aligned}
 N_2 &= \frac{1}{2}\xi(2\xi - \zeta - 2)(1 - \zeta) - \frac{1}{15}N_{16} \\
 N_3 &= \frac{1}{2}\eta(2\xi - \zeta - 2)(1 - \zeta) - \frac{1}{15}N_{16} \\
 N_4 &= -\frac{1}{2}(1 - \xi - \eta)(2\xi + 2\eta - \zeta)(1 + \zeta) - \frac{1}{15}N_{16} \\
 N_5 &= \frac{1}{2}\xi(2\xi + \zeta - 2)(1 + \zeta) - \frac{1}{15}N_{16} \\
 N_6 &= \frac{1}{2}\eta(2\eta + \zeta - 2)(1 + \zeta) - \frac{1}{15}N_{16} \\
 N_7 &= 2\xi(1 - \xi - \eta)(1 - \zeta) - \frac{1}{15}N_{16} \\
 N_8 &= 2\xi\eta(1 - \zeta) - \frac{1}{15}N_{16} \\
 N_9 &= 2\eta(1 - \xi - \eta)(1 - \zeta) - \frac{1}{15}N_{16} \\
 N_{10} &= 2\xi(1 - \xi - \eta)(1 + \zeta) - \frac{1}{15}N_{16} \\
 N_{11} &= 2\xi\eta(1 + \zeta) - \frac{1}{15}N_{16} \\
 N_{12} &= 2\eta(1 - \xi - \eta)(1 + \zeta) - \frac{1}{15}N_{16} \\
 N_{13} &= (1 - \xi - \eta)(1 - \zeta^2) - \frac{1}{15}N_{16} \\
 N_{14} &= \xi(1 - \zeta^2) - \frac{1}{15}N_{16} \\
 N_{15} &= \eta(1 - \zeta^2) - \frac{1}{15}N_{16} \\
 N_{16} &= \frac{19683}{4096}\xi\eta(1 - \xi - \eta)(2\xi + 2\eta \\
 &\quad + \zeta)(2\xi - \zeta - 2)(2\eta - \zeta - 2) \\
 &\quad (2\xi + 2\eta - \zeta) \\
 &\quad (2\xi + \zeta - 2)(2\eta + \zeta - 2)(1 - \zeta^2)
 \end{aligned} \tag{82}$$

References

Abraham FF, Bernstein N, Broughton JQ, Hess D (2000) Dynamic fracture of silicon: concurrent simulation of quantum electrons, classical atoms, and the continuum solid. *MRS Bull* 25:27–32

Ando T, Li X, Nakao S, Kasai T, Tanaka H, Shikida M, Sato K (2005) Fracture toughness measurement of thin-film silicon. *Fatigue Fract Eng Mater Struct* 28:687–694

Belytschko T (1983) An overview of semidiscretization and time integration procedures. *Computational methods for transient analysis* (A 84-29160 12-64). North Holland, Amsterdam, pp 1–65

Belytschko T, Black T (1999) Elastic crack growth in finite elements with minimal remeshing. *Int J Numer Methods Eng* 45:601–620

Belytschko T, Möes N, Usui S, Parimi C (2001) Arbitrary discontinuities in finite elements. *Int J Numer Methods Eng* 50:993–1013

Bogue R (2007) MEMS sensors: past, present and future. *Sens Rev* 27:7–13

Boyd EJ, Li L, Blue R, Uttamchandani D (2013) Measurement of the temperature coefficient of Young’s modulus of single crystal silicon and 3C silicon carbide below 273 K using micro-cantilevers. *Sens Actuators A Phys* 198:75–80

Buehler MJ, van Duin ACT, Goddard WA III (2006) Multiparadigm modeling of dynamical crack propagation in silicon using a reactive force field. *Phys Rev Lett* 96:095505

Chasiotis I, Cho SW, Jonnalagadda K (2006) Fracture toughness and subcritical crack growth in polycrystalline silicon. *J Appl Mech* 73:714–722

de Brito Mota F, Justo JF, Fazzio A (1998) Structural properties of amorphous silicon nitride. *Phys Rev B* 58:8323

Demetriou MD, Launey ME, Garrett G, Schramm JP, Hofmann DC, Johnson WL, Ritchie RO (2010) A damage-tolerant glass. *Nat Mater* 10:123–128

Ericson F, Schweitz JÅ (1990) Micromechanical fracture strength of silicon. *J Appl Phys* 68:5840

Fan H, Li S (2015) Multiscale cohesive zone modeling of crack propagations in polycrystalline solids. *GAMM Mitteilungen* 38:268–284

Fan H, Shi C, Li S (2013) Application of multiscale process zone model to simulate fracture in polycrystalline solids. *J Multiscale Model* 5:1350015

Fitzgerald AM, Dauskardt RH, Kenny TW (2000) Fracture toughness and crack growth phenomena of plasma-etched single crystal silicon. *Sens Actuators A Phys* 83:194–199

Hauch JA, Holland D, Marder MP, Swinney HL (1999) Dynamic fracture in single crystal silicon. *Phys Rev Lett* 82:3823–3826

He M, Li S (2012) An embedded atom hyperelastic constitutive model and multiscale cohesive finite element method. *Comput Mech* 49:337–355

Hopcroft MA, Nix WD, Kenny TW (2010) What is the Young’s modulus of silicon? *J Microelectromech Syst* 19:229–238

Izumi S, Sakai S (2004) Internal displacement and elastic properties of the silicon Tersoff potential. *JSME Int J Ser A Solid Mech Mater Eng* 47:54–61

Jensen KF (1999) Microchemical systems: status, challenges, and opportunities. *AIChE J* 45:2051–2054

- Kang K, Cai W (2007) Brittle and ductile fracture of semiconductor nanowires—molecular dynamics simulations. *Philos Mag* 87:2169–2189
- Karlssoon S, Jonson B, Stålhandske C (2010) The technology of chemical glass strengthening—a review. *Glass Technol Eur J Glass Sci Technol Part A* 51:41–54
- Khoei AR, DorMohammadi H (2012) Validity and size-dependency of Cauchy–Born hypothesis with Tersoff potential in silicon nano-structures. *Comput Mater Sci* 63:168–177
- Khoei AR, DorMohammadi H, Aramoon A (2014) A temperature-related boundary Cauchy–Born method for multi-scale modeling of silicon nano-structures. *Phys Lett A* 378:551–560
- Koike A, Akiba S, Sakagami T, Hayashi K, Ito S (2012) Difference of cracking behavior due to Vickers indentation between physically and chemically tempered glasses. *J Non Cryst Solids* 358:3438–3444
- Li X, Kasai T, Nakao S, Tanaka H, Ando T, Shikida M, Sato K (2005) Measurement for fracture toughness of single crystal silicon film with tensile test. *Sens Actuators A Phys* 119:229235
- Li S, Zeng X, Ren B, Qian J, Zhana J, Jha AK (2012) An atomistic-based interphase zone model for crystalline solids. *Comput Methods Appl Mech Eng* 229:87–109
- Li S, Ren B, Minaki H (2014) Multiscale crystal defect dynamics: a dual-lattice process zone model. *Philos Mag* 94:1414–1450. doi:10.1080/14786435.2014.887859
- Liu L, Li S (2012) A finite temperature multiscale interphase zone model and simulations of fracture. *J Eng Mater Technol* 134:31014
- Liu X, Li S, Sheng N (2008) A cohesive finite element for quasi-continua. *Comput Mech* 42:543–553
- Madenci E, Oterkus E (2014) *Peridynamics theory and its applications*. Springer, Berlin
- McMeeking RM, Evans AG (1982) Mechanics of transformation-toughening in brittle materials. *J Am Ceram Soc* 65:242–246
- Munetoh S, Motooka T, Moriguchi K, Shintani A (2007) Interatomic potential for SiO systems using Tersoff parameterization. *Comput Mater Sci* 39:334–339
- Nakao S, Ando T, Shikida M, Sato K (2008) Effect of temperature on fracture toughness in a single-crystal-silicon film and transition in its fracture mode. *J Micromech Microeng* 18:15026
- Park HS, Klein PA (2008) A surface Cauchy–Born model for silicon nanostructures. *Comput Methods Appl Mech Eng* 197:3249–3260
- Petersen KE (1982) Silicon as a mechanical material. *Proc IEEE* 70:420–457
- Plimpton S (1995) Fast parallel algorithms for short-range molecular dynamics. *J Comput Phys* 117:1–19
- Qian J, Li S (2010) Application of multiscale cohesive zone model to simulate fracture in polycrystalline solids. *J Eng Mater Technol* 133:11010
- Raghunathan AV, Park JH, Alurua NR (2007) Interatomic potential-based semiclassical theory for Lennard-Jones fluids. *J Chem Phys* 127:174701
- Shegal J, Ito S (1998) A new low-brittleness glass in the soda-lime-silica glass family. *J Am Ceram Soc* 81:2485–2488
- Shet C, Chandra N (2002) Analysis of energy balance when using cohesive zone models to simulate fracture processes. *J Eng Mater Technol* 124:440–450
- Siling SA (2000) Reformulation of elasticity theory for discontinuities and long-range forces. *J Mech Phys Solids* 48:175–209
- Siling SA, Eptom M, Weckner O, Xu J, Askari A (2007) Peridynamics states and constitutive modeling. *J Elast* 88:51–184
- Stillinger FH, Weber TA (1985) Computer simulation of local order in condensed phases of silicon. *Phys Rev B* 31:5262–5271
- Sundararajan S, Bhushan B (2002) Development of AFM-based techniques to measure mechanical properties of nanoscale structures. *Sens Actuators A Phys* 101:338–351
- Sunyk R, Steinmann P (2003) On higher gradients in continuum-atomistic modelling. *Int J Solids Struct* 40(24):6877–6896
- Swiler TP, Simmons JH, Wright AC (1995) Molecular dynamics study of brittle fracture in silica glass and cristobalite. *J Non Cryst Solids* 182:68–77
- Tadmor EB, Miller RE (2011) *Modeling materials—continuum, atomistic and multiscale technologies*. Cambridge University Press, Cambridge
- Tadmor EB, Smith GS, Bernstein N, Kaxiras E (1999) Mixed finite element and atomistic formulation for complex crystals. *Phys Rev B* 59:235–245
- Tamai J, Chen I-W, Yamamoto Y, Komatsu M, Komeya K, Kim DK, Wakihara T, Meguro T (2006) Fracture resistance and contact damage of TiN particle reinforced Si₃N₄ ceramics. *J Ceram Soc Jpn* 114:1049–1053
- Tang Z, Zhao H, Li G, Aluru NR (2006) Finite-temperature quasi-continuum method for multiscale analysis of silicon nanostructures. *Phys Rev B* 74:64110
- Terao R, Tatami J, Meguro T, Komeya K (2002) Fracture behavior of AlN ceramics with rare earth oxides. *J Eur Ceram Soc* 22:1051–1059
- Tersoff J (1988) New empirical approach for the structure and energy of covalent systems. *Phys Rev B* 37:6991–6999
- Tersoff J (1988) Empirical interatomic potential for silicon with improved elastic properties. *Phys Rev B* 38:9902–9905
- Tersoff J (1989) Modeling solid-state chemistry: interatomic potentials for multicomponent systems. *Phys Rev B* 39:5566–5568
- Varshneya AK (2010) Chemical strengthening of glass: lessons learned and yet to be learned. *Int J Appl Glass Sci* 1:131–142
- Volokh KY (2004) Comparison between cohesive zone models. *Commun Numer Methods Eng* 20:845–856
- Wong B, Holbrook RJ (1987) Microindentation for fracture and stresscorrosion cracking studies in singlecrystal silicon. *J Electrochem Soc* 134:2254–2256
- Xu XP, Needleman A (1994) Numerical simulations of fast crack growth in brittle solids. *J Mech Phys Solids* 42:1397–1434
- Zeng X, Li S (2010) A multiscale cohesive zone model and simulations of fractures. *Comput Methods Appl Mech Eng* 199:547–556
- Zeng X, Li S (2012) Application of a multiscale cohesive zone method to model composite materials. *Int J Multiscale Comput Eng* 10:391–405